

Deformation of Ne isotopes in the island-of-inversion region

Takenori Sumi,¹ Kosho Minomo,¹ Shingo Tagami,¹ Masaaki Kimura,² Takuma Matsumoto,¹ Kazuyuki Ogata,³ Yoshifumi R. Shimizu,¹ and Masanobu Yahiro¹

¹*Department of Physics, Kyushu University, Fukuoka 812-8581, Japan*

²*Creative Research Institution (CRIS), Hokkaido University, Sapporo 001-0021, Japan*

³*Research Center of Nuclear Physics (RCNP), Osaka University, Ibaraki 567-0047, Japan*

(Dated: January 13, 2012)

The deformation of Ne isotopes in the island-of-inversion region is determined by the double-folding model with the Melbourne g -matrix and the density calculated by the antisymmetrized molecular dynamics (AMD). The double-folding model reproduces, with no adjustable parameter, the measured reaction cross sections for the scattering of $^{28-32}\text{Ne}$ from ^{12}C at 240 MeV/nucleon. The quadrupole deformation thus determined is around 0.4 in the island-of-inversion region and ^{31}Ne is a halo nuclei with large deformation. We propose the Woods-Saxon model with a suitably chosen parameterization set and the deformation given by the AMD calculation as a convenient way of simulating the density calculated directly by the AMD. The deformed Woods-Saxon model provides the density with the proper asymptotic form. The pairing effect is investigated, and the importance of the angular momentum projection for obtaining the large deformation in the island-of-inversion region is pointed out.

PACS numbers: 21.10.Gv, 21.60.Ev, 21.60.Gx, 25.60.Dz

I. INTRODUCTION

Exploring the so-called “Island of inversion” is one of the most important current subjects in nuclear physics. The term “Island of inversion (IOI)” was first introduced by Warburton [1] to the region of unstable nuclei from ^{30}Ne to ^{34}Mg . In the region, the low excitation energies and the large $B(E2)$ values of the first excited states suggest strong deformations [2–6]. This indicates that the $N = 20$ magic number is no longer valid. This novel quantum property has triggered extensive experimental and theoretical studies on the IOI region.

Another important progress of research on unstable nuclei is the discovery of the halo structure [7–9]. Very recently, the interaction cross section σ_I was measured by Takechi *et al.* [10] for the scattering of $^{28-32}\text{Ne}$ at 240 MeV/nucleon and it was shown that σ_I is quite large for ^{31}Ne . A halo structure of ^{31}Ne was reported by the experiment on the one-neutron removal reaction [11]. This is the heaviest halo nucleus in the present stage suggested experimentally. The nucleus resides in the IOI region. The reaction cross section σ_R (or σ_I) and the nucleon-removal cross section with radioactive beams are thus important experimental tools for exploring unstable nuclei [7–12]. For the scattering of unstable nuclei at intermediate energies, σ_I agrees with σ_R exactly or nearly, since projectile excitations to its discrete excited states do not exist or small even if they exist. This is discussed in this paper.

A useful theoretical tool of analyzing σ_R is the microscopic optical potential constructed by the double-folding model (DFM) with the g -matrix effective nucleon-nucleon (NN) interaction [13–21], when the projectile breakup is weak. For the nucleon-nucleus scattering, the single-folding model with the Melbourne g -matrix well reproduces the data on σ_R and the elastic-scattering cross

section systematically [20]. For ^{31}Ne scattering from ^{12}C at 240 MeV/nucleon, the breakup cross section is about 1% of σ_R [22]. The DFM is hence reliable also for other projectiles $^{20-32}\text{Ne}$, since ^{31}Ne is a most-weakly bound system among them.

In the DFM, the microscopic optical potential is constructed by folding the g -matrix with projectile and target densities. The density profile changes, if it is deformed. The elongation makes the surface diffuseness and the root-mean-square (RMS) radius effectively larger and eventually enhances σ_R . The amount of deformation is thus important. Nuclei in the IOI region are spherical or only weakly deformed in the Skyrme and/or Gogny HF (HFB) calculations; see, e.g., Refs. [23, 24]. It is even pointed out that the observed large $B(E2; 2^+ \rightarrow 0^+)$ values can be understood as a large amplitude vibration around the spherical shape [25]. In such a situation, the additional correlations by the angular momentum projection (AMP) often leads to possible deformed shapes; see Ref. [26] for Ne isotopes.

Recently a systematic analysis was made by the antisymmetrized molecular dynamics (AMD) with the Gogny D1S interaction for both even and odd N nuclei in the IOI region [27, 28]. The AMP-AMD calculations, i.e. the AMD calculation with the AMP performed, yields rather large deformations. This is consistent with the AMP-HFB calculations [24, 26]. A consistent picture of even and odd isotopes has been obtained by the AMP-AMD approach, where the n -particle m -hole excitations of the Nilsson orbits play important roles to determine deformed configurations. Although it is difficult to distinguish the dynamic shape-fluctuation and static deformation in these light mass nuclei, one may use the deformed shape suggested by the AMD calculation to see its effect on σ_R . Very recently the Woods-Saxon mean-field model with the deformation obtained by the AMP-AMD cal-

culation was applied for $^{28-32}\text{Ne}$ and the DFM with the density of the mean-field model was successful in reproducing the data on σ_R in virtue of the deformation [29].

In principle, we can calculate the double-folding potential directly by using the nucleon density calculated with the AMD. The nucleon density is, however, inaccurate in the asymptotic region, since each nucleon is described by a Gaussian wave packet in the AMD. Very lately we proposed a way of making a tail correction to the AMD density [30]. Although the calculation based on the resonating group method is quite time-consuming, it was applied to ^{31}Ne [30], since the correction is most significant for ^{31}Ne that is a most-weakly bound system among $^{20-32}\text{Ne}$. The tail correction to σ_R is about 3 % for ^{31}Ne . The DFM with the tail-corrected density reproduces the measured σ_R for ^{31}Ne , whereas the DFM without the tail correction underestimates the data slightly.

In this paper, we analyze the reaction cross section for the scattering of $^{20-32}\text{Ne}$ from a ^{12}C target at 240 MeV/nucleon by using the DFM with the Melbourne g -matrix in order to determine deformations of $^{20-32}\text{Ne}$ systematically. Here the projectile density is constructed either (I) by the AMP-AMD calculation with the Gogny D1S interaction or (II) by the Woods-Saxon model with the deformation obtained by the AMP-AMD calculation. Model I has no adjustable parameter, but the density is inaccurate in the asymptotic region. Model II provides the nucleon density with the proper asymptotic form, but the model includes potential parameters. As the potential parameter set, we use the parameter set recently proposed by R. Wyss [31]. This set is intended to reproduce the spectroscopic properties of high-spin states from light to heavy deformed nuclei, e.g., the quadrupole moments and the moments of inertia, and at the same time the RMS radii crucial for the present analysis.

Models I and II yield almost the same σ_R for $^{24-29}\text{Ne}$ that have large one-neutron separation energies. Furthermore, this agreement is seen for ^{31}Ne , when the tail correction is made in Model I. This indicates that Model II is a handy way of simulating results of Model I with the tail correction. Model II is quite practical compared with Model I with the tail correction that requires time-consuming calculations. Model I with the tail correction and Model II reproduce the measured σ_R of $^{20,28-32}\text{Ne}$. The deformation of $^{28-32}\text{Ne}$ is then definitely determined through this analysis. This analysis also yields a reasonable prediction for the deformation of $^{21-27}\text{Ne}$. We also confirm that ^{31}Ne is a halo nucleus with large deformation. Furthermore, we analyze the AMP effect and the pairing effect on σ_R by using Model II.

The theoretical framework is presented in Sec. II. We explain the DFM, the AMP-AMD and the Woods-Saxon mean-field model. We present a handy way of making a center-of-mass (CM) correction to the density of the mean-field model. We also show in Sec. II that the dynamical deformation effect and the reorientation effect neglected in the present DFM are small. This indicates that $\sigma_I \approx \sigma_R$. Numerical results are shown in Sec. III.

Section IV is devoted to summary.

II. THEORETICAL FRAMEWORK

A. Double folding model

We start with the many-body Schrödinger equation with the realistic NN interaction v_{ij} for the scattering of projectile (P) on target (T):

$$(T_R + h_P + h_T + \sum_{i \in P, j \in T} v_{ij} - E) \Psi^{(+)} = 0 , \quad (1)$$

where E is the energy of the total system, T_R is the kinetic energy of relative motion between P and T, and h_P (h_T) is the internal Hamiltonian of P (T). The multiple-scattering theory [32, 33] for nucleon-nucleus scattering was extended to nucleus-nucleus scattering [34]. According to the theory, Eq. (1) is approximated into

$$(T_R + h_P + h_T + \sum_{i \in P, j \in T} \tau_{ij} - E) \hat{\Psi}^{(+)} = 0 , \quad (2)$$

where τ_{ij} is the effective NN interaction in the nuclear medium. The Brueckner g matrix has often been used as such τ_{ij} in many applications; see for example Refs. [13–21]. The g matrix interaction includes the nuclear-medium effect, but not the effect of collective excitations induced by the surface vibration and the rotation of finite nucleus, since the interaction is evaluated in the nuclear matter. The effect of collective excitations is small as shown in Sec. II E.

In the scattering analyzed here, furthermore, the projectile-breakup effect is small, since the target is light and E is large. This is explicitly shown in Sec. III B. In this situation the DFM becomes reliable. In the model, the potential U between P and T consists of the direct and exchange parts, U^D and U^{EX} , defined by [35, 36]

$$U^{\text{DR}}(\mathbf{R}) = \sum_{\mu, \nu} \int \rho_P^\mu(\mathbf{r}_P) \rho_T^\nu(\mathbf{r}_T) g_{\mu\nu}^{\text{DR}}(s; \rho_{\mu\nu}) d\mathbf{r}_P d\mathbf{r}_T , \quad (3)$$

$$U^{\text{EX}}(\mathbf{R}) = \sum_{\mu, \nu} \int \rho_P^\mu(\mathbf{r}_P, \mathbf{r}_P + \mathbf{s}) \rho_T^\nu(\mathbf{r}_T, \mathbf{r}_T - \mathbf{s}) \times g_{\mu\nu}^{\text{EX}}(s; \rho_{\mu\nu}) \exp[i\mathbf{K}(\mathbf{R}) \cdot \mathbf{s}/M] d\mathbf{r}_P d\mathbf{r}_T , \quad (4)$$

where $\mathbf{s} = \mathbf{r}_P - \mathbf{r}_T + \mathbf{R}$ for the coordinate \mathbf{R} of P from T. Indices μ and ν stand for the z -component of isospin ; $\mu = 1/2$ ($\nu = 1/2$) means neutron and $\mu = -1/2$ ($\nu = -1/2$) does proton. The original form of U^{EX} is a non-local function of \mathbf{R} , but it has been localized in Eq. (4) with the local semi-classical approximation [15] in which P is assumed to propagate as a plane wave with the local momentum $\hbar\mathbf{K}(\mathbf{R})$ within a short range of the NN interaction, where $M = AA_T/(A + A_T)$ for the mass number A (A_T) of P (T). The validity of this localization is shown in Ref. [37].

The direct and exchange parts, $g_{\mu\nu}^{\text{DR}}$ and $g_{\mu\nu}^{\text{EX}}$, of the effective NN (g -matrix) interaction are assumed to depend on the local density

$$\rho_{\mu\nu} = \rho_{\text{P}}^\mu(\mathbf{r}_{\text{P}} + \mathbf{s}/2) + \rho_{\text{T}}^\nu(\mathbf{r}_{\text{T}} - \mathbf{s}/2) \quad (5)$$

at the midpoint of the interacting nucleon pair. The direct and exchange parts, $g_{\mu\nu}^{\text{DR}}$ and $g_{\mu\nu}^{\text{EX}}$, are described by

$$g_{\mu,\nu,T_z=\pm 1}^{\text{DR}}(s; \rho_{\mu\nu}) = \frac{1}{4} \sum_S \hat{S}^2 g_{\mu\nu}^{S1}(s; \rho_{\mu\nu}) \delta_{T_z}^{\mu+\nu}, \quad (6)$$

$$g_{\mu,\nu,T_z=0}^{\text{DR}}(s; \rho_{\mu\nu}) = \frac{1}{8} \sum_{S,T} \hat{S}^2 g_{\mu\nu}^{ST}(s; \rho_{\mu\nu}) \delta_{T_z}^{\mu+\nu}, \quad (7)$$

$$g_{\mu,\nu,T_z=\pm 1}^{\text{EX}}(s; \rho_{\mu\nu}) = \frac{1}{4} \sum_S (-1)^{S+1} \hat{S}^2 g_{\mu\nu}^{S1}(s; \rho_{\mu\nu}) \delta_{T_z}^{\mu+\nu}, \quad (8)$$

$$g_{\mu,\nu,T_z=0}^{\text{EX}}(s; \rho_{\mu\nu}) = \frac{1}{8} \sum_{S,T} (-1)^{S+T} \hat{S}^2 g_{\mu\nu}^{ST}(s; \rho_{\mu\nu}) \delta_{T_z}^{\mu+\nu}, \quad (9)$$

with $\hat{S} = \sqrt{2S+1}$, in terms of the spin-isospin components $g_{\mu\nu}^{ST}$ of the g matrix interaction. As for the g matrix interaction, we take a sophisticated version of the Melbourne interaction [20] that is constructed from the Bonn-B NN potential [38]. In actual calculations, the relativistic kinematics is taken for T_R and E .

B. AMD framework and inputs for the reaction calculations

The framework and calculational procedure of the AMD in this study are common to those of Ref. [28], and the reader is directed to it for more detail. The Hamiltonian of the AMD is given as

$$H = T_{\text{tot}} + \sum_{i < j} \bar{v}_{ij} - T_{\text{cm}}. \quad (10)$$

The Gogny D1S [39] is used as an effective nucleon-nucleon interaction \bar{v}_{ij} ; here note that the Coulomb part of \bar{v}_{ij} is approximated by a sum of twelve Gaussians. T_{tot} and T_{cm} represent the kinetic energies of nucleons and center-of-mass motion, respectively.

The variational wave function is a parity-projected wave function and the intrinsic wave function is a Slater determinant of nucleon wave packets,

$$\Phi^\pi = P^\pi \mathcal{A} \{ \varphi_1, \varphi_2, \dots, \varphi_A \}, \quad (11)$$

where P^π is the parity projector. The nucleon wave packet φ_i is a direct product of spatial ϕ_i , spin χ_i and isospin ξ_i parts,

$$\varphi_i = \phi_i(\mathbf{r}) \chi_i \xi_i, \quad (12)$$

$$\phi_i(\mathbf{r}) = \prod_{\sigma=x,y,z} \left(\frac{2\nu_\sigma}{\pi} \right)^{1/4} \exp \left\{ -\nu_\sigma \left(r_\sigma - \frac{Z_{i\sigma}}{\sqrt{\nu_\sigma}} \right)^2 \right\}, \quad (13)$$

$$\chi_i = \alpha_{i,\uparrow} \chi_\uparrow + \alpha_{i,\downarrow} \chi_\downarrow, \quad \xi_i = \text{p or n}, \quad (14)$$

where the centroids of Gaussian wave packets \mathbf{Z}_i , the width of Gaussian ν_σ and the spin direction $\alpha_{i,\uparrow}$ and $\alpha_{i,\downarrow}$ are the parameters determined variationally as explained below. Note that the center-of-mass wave function is analytically separable from the variational wave function Eq. (11):

$$\Phi^\pi = \Phi_{\text{cm}} \Phi_{\text{int}}, \quad (15)$$

$$\Phi_{\text{cm}} = \prod_{\sigma=x,y,z} \left(\frac{2A\nu_\sigma}{\pi} \right)^{1/4} \exp \left\{ -A\nu_\sigma \left(X_\sigma - \frac{Z_{\text{cm},\sigma}}{\sqrt{A\nu_\sigma}} \right)^2 \right\}, \quad (16)$$

$$\mathbf{Z}_{\text{cm}} = \frac{1}{\sqrt{A}} \sum_{i=1}^A \mathbf{Z}_i, \quad (17)$$

where \mathbf{X} represents the center-of-mass coordinate. Usually, \mathbf{Z}_{cm} defined by Eq. (17) can be set to zero without loss of generality. This is common to the angular momentum projection and GCM calculation, and all quantities used as inputs of reaction calculation are free from the spurious center-of-mass motion.

The parameters in Eq. (11) are determined using the frictional cooling method to minimize the total energy under the constraint on the matter quadrupole deformation parameter $\bar{\beta}$. Here the quadrupole deformation parameters are defined as,

$$\frac{\langle x^2 \rangle^{1/2}}{[\langle x^2 \rangle \langle y^2 \rangle \langle z^2 \rangle]^{1/6}} = \exp \left[\sqrt{\frac{5}{4\pi}} \bar{\beta} \cos \left(\bar{\gamma} + \frac{2\pi}{3} \right) \right], \quad (18)$$

$$\frac{\langle y^2 \rangle^{1/2}}{[\langle x^2 \rangle \langle y^2 \rangle \langle z^2 \rangle]^{1/6}} = \exp \left[\sqrt{\frac{5}{4\pi}} \bar{\beta} \cos \left(\bar{\gamma} - \frac{2\pi}{3} \right) \right], \quad (19)$$

$$\frac{\langle z^2 \rangle^{1/2}}{[\langle x^2 \rangle \langle y^2 \rangle \langle z^2 \rangle]^{1/6}} = \exp \left[\sqrt{\frac{5}{4\pi}} \bar{\beta} \cos \bar{\gamma} \right]. \quad (20)$$

Here, $\langle x^2 \rangle$, $\langle y^2 \rangle$ and $\langle z^2 \rangle$ are calculated from Φ_{int} in the intrinsic frame that is so chosen to satisfy the relation $\langle x^2 \rangle \leq \langle y^2 \rangle \leq \langle z^2 \rangle$. The constraint is imposed on the value of $\bar{\beta}$ from 0 to 1.0 with the interval of 0.025. Since we do not make any assumption on the spatial symmetry of the wave function and do not impose any constraint on $\bar{\gamma}$, it has an optimal value for each given value of $\bar{\beta}$.

After the variation, we perform the angular momentum projection for each value of $\bar{\beta}$,

$$\Phi_{MK}^{J\pi}(\bar{\beta}) = P_{MK}^J \Phi_{\text{int}}^\pi(\bar{\beta}), \quad (21)$$

$$P_{MK}^{J\pi} = \frac{2J+1}{8\pi^2} \int d\Omega D_{MK}^{J*}(\Omega) R(\Omega), \quad (22)$$

where $D_{MK}^J(\Omega)$ and $R(\Omega)$ are Wigner's D function and rotation operator, respectively. The integrals over three Euler angles Ω in Eq. (22) are performed numerically.

The AMD calculation is completed by performing the GCM. The wave functions that have the same parity and

angular momentum (J, M) are superposed as

$$\Phi_n^{J\pi} = \sum_{K=-J}^J \sum_{\bar{\beta}} c_{nK}(\bar{\beta}) \Phi_{MK}^{J\pi}(\bar{\beta}). \quad (23)$$

In other words, K and $\bar{\beta}$ are the generator coordinates in this calculation. The coefficients $c_{nK}(\bar{\beta})$ are determined by solving the Hill-Wheeler equation.

$$\sum_{\bar{\beta}' K'} H_{KK'}(\bar{\beta}, \bar{\beta}') c_{nK'}(\bar{\beta}') = E_n \sum_{\bar{\beta}' K'} N_{KK'}(\bar{\beta}, \bar{\beta}') c_{nK'}(\bar{\beta}'), \quad (24)$$

$$\left\{ \begin{array}{l} N_{KK'}(\bar{\beta}, \bar{\beta}') \\ H_{KK'}(\bar{\beta}, \bar{\beta}') \end{array} \right\} = \langle \Phi_{MK}^{J\pi}(\bar{\beta}) | \left\{ \begin{array}{l} 1 \\ H \end{array} \right\} | \Phi_{MK'}^{J\pi}(\bar{\beta}') \rangle. \quad (25)$$

The ground state wave function $\Phi_{g.s.}^{J\pi}$ obtained by this procedure is used in the discussion of Sec. III.

For the reaction calculation, two types of applications are performed. One is to use the deformation parameters $\bar{\beta}$ and $\bar{\gamma}$ as inputs of deformed Woods-Saxon potential. We assign the deformation of the AMD wave function by picking up a GCM basis wave function that has the maximum overlap with the ground state wave function, $|\langle \Phi_{g.s.}^{JM\pi} | \Phi_{MK}^{J\pi}(\bar{\beta}) \rangle|^2$. And then we define the deformation of AMD wave function as equal to $\bar{\beta}$ and corresponding $\bar{\gamma}$.

The other is the direct use of the nucleon density calculated from the ground state wave function as an input of the double-folding potential,

$$\rho_{JMJM'}(\mathbf{r}) = \langle \Phi_{g.s.}^{JM\pi} | \sum_i \delta(\mathbf{r}_i - \mathbf{X} - \mathbf{r}) | \Phi_{g.s.}^{JM'\pi} \rangle, \quad (26)$$

$$= \sum_{\lambda=0}^{2J} \rho_{JJ}^{(\lambda)}(r) (JM' \lambda \mu | JM) Y_{\lambda\mu}^*(\hat{r}), \quad (27)$$

where the summation of λ in Eq. (27) runs for even numbers. When only $\rho_{JJ}^{(\lambda=0)}$ is taken in the double-folding potential, the resultant folding potential becomes spherical. This approximation is often used as a standard manner in the DFM. The validity of this approximation is shown in Sec. II E.

C. Woods-Saxon mean-field model

We also perform DFM calculations with resultant density calculated by the simple mean-field model based on the Woods-Saxon potential. Sophisticated AMD calculation is a powerful tool but it costs much time to obtain reliable information, so, we take a deformed Woods-Saxon model for alternative approach and for further investigation. As shown later, in many cases of Ne isotope induced reaction cross section, the deformed Woods-Saxon model gives results consistent with the AMD calculation if one uses the consistent deformation.

The deformed Woods-Saxon potential in Schrödinger equation is composed of the central and spin-orbit part, which have the following forms:

$$V_c(\mathbf{r}) = \frac{V_0}{1 + \exp[\text{dist}_{\Sigma}(\mathbf{r})/a]}, \quad (28)$$

$$V_{so}(\mathbf{r}) = \lambda_{so} \left(\frac{\hbar}{2m_{\text{red}}c} \right)^2 \nabla V_c(\mathbf{r}) \cdot \left(\boldsymbol{\sigma} \times \frac{1}{i} \nabla \right), \quad (29)$$

where $m_{\text{red}} = m(A-1)/A$ and $\text{dist}_{\Sigma}(\mathbf{r})$ represents a distance between a given point \mathbf{r} and the deformed surface Σ specified by the radius,

$$R(\theta, \phi; \boldsymbol{\alpha}) = R_0 c_v(\boldsymbol{\alpha}) \left[1 + \sum_{\lambda\mu} \alpha_{\lambda\mu}^* Y_{\lambda\mu}(\theta, \phi) \right], \quad (30)$$

with the deformation parameters $\boldsymbol{\alpha} \equiv \{\alpha_{\lambda\mu}\}$. The constant $c_v(\boldsymbol{\alpha})$ is introduced to guarantee the volume conservation of nucleus. A set of deformation parameters used in the present work is $(\beta_2, \gamma, \beta_4)$ [40], which are related to $(\alpha_{2\mu}, \alpha_{4\mu})$ by

$$\left\{ \begin{array}{l} \alpha_{20} = \beta_2 \cos \gamma, \\ \alpha_{22} = \alpha_{2-2} = -\frac{1}{\sqrt{2}} \beta_2 \sin \gamma, \\ \alpha_{40} = \frac{1}{6} \beta_4 (5 \cos^2 \gamma + 1), \\ \alpha_{42} = \alpha_{4-2} = -\sqrt{\frac{5}{6}} \beta_4 \cos \gamma \sin \gamma, \\ \alpha_{44} = \alpha_{4-4} = \sqrt{\frac{35}{72}} \beta_4 \sin^2 \gamma, \end{array} \right. \quad (31)$$

where note that the other $\alpha_{\lambda\mu}$ are zero.

As for the parameter set of the Woods-Saxon potential, i.e., the potential depth V_0 , the nuclear radius R_0 , and the diffuseness parameter a of the central potential, as well as those for the spin-orbit potential, we take the one provided recently by R. Wyss [31] (see Ref. [41] for the actual values of parameters). For proton, the Coulomb potential created by charge $(Z-1)e$ that has a uniform distribution inside the surface Σ is added to Eq. (28); more detailed description are explained in e.g. Refs. [42].

The deformation parameters in the Woods-Saxon potential are determined by the standard Strutinsky (microscopic-macroscopic) method [43, 44], where the pairing correlation is included within the BCS approximation. The monopole pairing interaction is used and its strength is determined according to the smoothed pairing gap method. As for the macroscopic part energy, the liquid-drop model of Ref. [45] is employed. The Ne isotopes in the IOI region studied in the present work are sitting near the drip line. In such a case the standard Strutinsky method has problems related to the continuum single-particle states. Recently the problems are solved by using the so-called Kruppa prescription [46]. We have employed this improved method for the calculation of both the shell correction and the pairing correlation (Kruppa-BCS method).

As it is discussed in the following sections, we utilize different models for the analysis of reaction cross sections.

In order to compare the deformation in different models, it is necessary to transform the deformation parameters defined within each model, e.g., between $(\bar{\beta}, \bar{\gamma})$ in the AMD model and $(\beta_2, \gamma, \beta_4)$ in the Woods-Saxon model. This has been done in the following way. The deformed surface in Eq. (30) defines the deformation parameter in the Woods-Saxon potential. We define the uniform density with the sharp cut surface Σ ,

$$\rho_{\text{uni}}(\mathbf{r}) \equiv \rho_0 \theta(R(\theta, \phi; \boldsymbol{\alpha}) - r), \quad (32)$$

where ρ_0 is the average density and $\theta(x)$ is a step function, and calculate the expectation value with it, e.g.,

$$\langle x^2 \rangle_{\text{uni}} = \int x^2 \rho_{\text{uni}}(\mathbf{r}) d\mathbf{r}. \quad (33)$$

For a given AMD deformation parameters $(\bar{\beta}, \bar{\gamma})$, the ratio of the AMD expectation values $\langle x^2 \rangle : \langle y^2 \rangle : \langle z^2 \rangle$ is fixed according to Eqs. (18)–(20). Then the corresponding Woods-Saxon parameters $(\beta_2, \gamma, \beta_4)$ are defined to give the same shape, i.e., by the condition $\langle x^2 \rangle : \langle y^2 \rangle : \langle z^2 \rangle = \langle x^2 \rangle_{\text{uni}} : \langle y^2 \rangle_{\text{uni}} : \langle z^2 \rangle_{\text{uni}}$. This condition gives only two independent equations so that the (β_2, γ) is determined under some fixed value of β_4 . We set $\beta_4 = 0$ for simplicity in order to define the (β_2, γ) values corresponding to the AMD calculation. It is then found that the pairs $(\bar{\beta}, \bar{\gamma})$ and (β_2, γ) take similar values; see Table VI in Sec. III. We have checked that the results of the final reaction cross sections change very little (order of few mb), if we use the non-zero β_4 values within the range $-0.1 < \beta_4 < 0.1$.

In the actual calculation, the Woods-Saxon potential is diagonalized with the anisotropic harmonic oscillator basis, where the three frequencies, ω_i ($i = x, y, z$), are taken to be proportional to $1/\sqrt{\langle x_i^2 \rangle_{\text{uni}}}$, which is close to the optimal choice. As for the basis size, we have used the oscillator shells $N_{\text{osc}} = n_x + n_y + n_z = 18$ in most cases. However, the density distribution of the nucleus near the drip line extends considerably, and then we have checked the convergence of the results carefully by taking larger number of shells $N_{\text{osc}} \geq 20$ in such a case.

As in the Hartree-Fock (HF) or Hartree-Fock-Bogoliubov (HFB) approach, the occurrence of deformation in the Woods-Saxon model is a symmetry-breaking phenomenon. The many-body wave function Φ is then considered to be that in the intrinsic (body-fixed) frame [47], and so is the nucleon density calculated with Φ ,

$$\rho^{(\text{in})}(\mathbf{r}) = \langle \Phi | \sum_i \delta(\mathbf{r}_i - \mathbf{r}) | \Phi \rangle = \sum_{\alpha} |\varphi_{\alpha}(\mathbf{r})|^2 v_{\alpha}^2, \quad (34)$$

where $\varphi_{\alpha}(\mathbf{r})$ is the Woods-Saxon single-particle wave function and v_{α} is the BCS occupation probability (the free contributions should be subtracted when the Kruppa prescription is employed, see Refs. [46, 48] for details). Therefore the deformed density $\rho^{(\text{in})}(\mathbf{r}) = \rho^{(\text{in})}(r, \theta, \phi)$ cannot be directly used in the reaction calculation such

as the DFM that is done in the laboratory (space-fixed) frame.

One way to recover the spherical symmetry and transform the density in the intrinsic frame to that in the laboratory frame is to perform the angular momentum projection, as already explained in Eqs. (26)–(27) in the AMD framework. We have performed the projection calculation (without the CM correction, which is discussed in the next subsection) by using the method of Ref. [49] for the Woods-Saxon model with the BCS pairing correlation. It is found that the projected density $\rho_{JJ}^{(0)}(r)/\sqrt{4\pi}$, where $\rho_{JJ}^{(\lambda=0)}(r)$ is defined in the same way as in Eq. (27) and used in the DFM, is very similar to the following angle-averaged intrinsic density,

$$\rho_{\text{av}}^{(\text{in})}(r) = \frac{1}{4\pi} \int \rho^{(\text{in})}(r, \theta, \phi) \sin \theta d\theta d\phi. \quad (35)$$

In Fig. 1, they are compared for ${}^{30}\text{Ne}$. As it is clear, for both neutron and proton, the projected and angle-average densities are almost identical particularly in the tail region, while slight differences are observed in the inner region for large J values. This is rather general trend, and therefore, we use $\rho_{\text{av}}^{(\text{in})}(r)$ in place of $\rho_{JJ}^{(0)}(r)/\sqrt{4\pi}$ in the Woods-Saxon model for the ground state of Ne isotopes.

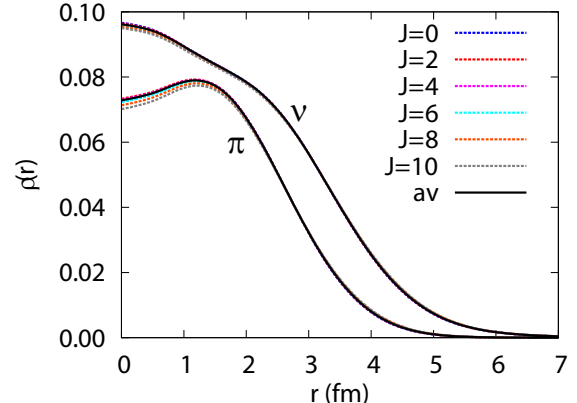


FIG. 1: (Color online) Comparison of the projected density, $\rho_{JJ}^{(0)}(r)/\sqrt{4\pi}$ with $J = 0, 2, \dots, 10$, and the angle-averaged intrinsic density, $\rho_{\text{av}}^{(\text{in})}(r)$ in Eq. (35), for the Woods-Saxon model in ${}^{30}\text{Ne}$. The deformation parameters are $\beta_2 = 0.4$ and $\gamma = \beta_4 = 0$, and the pairing gaps $\Delta_n = \Delta_p = 1$ MeV. The results are very similar also for the case with no pairing correlation.

In the view of static behaviour of deformed nuclei, using spherical part of deformed Woods-Saxon density, $\rho_{JJ}^{(0)}(r)/\sqrt{4\pi} \approx \rho_{\text{av}}(r)$, is well justified, but, this procedure doesn't justify that dynamical aspect of deformation is also negligible. As mentioned above, this point is argued in Sec. II E.

D. CM correction to nucleon density of the Woods-Saxon mean-field model

The projectile density is constructed with either the AMD or the Woods-Saxon model for Ne isotopes. In contrast to the AMD calculation, the CM motion is not excluded in the many-body wave function Φ in the Woods-Saxon model. We then extract the CM motion from Φ in the standard manner [50, 51] and propose a simple extraction prescription consistent with the standard manner.

The wave function Φ is approximated by a product of the CM part Φ_{cm} and the intrinsic part Φ_{int} :

$$\Phi = \Phi_{\text{cm}} \Phi_{\text{int}} \quad (36)$$

with

$$\Phi_{\text{cm}} = \left(\frac{A}{\pi b^2} \right)^{3/4} \exp \left[-\frac{A}{2b^2} X^2 \right] \quad (37)$$

for the CM coordinate \mathbf{X} and the size parameter b . The mean squared radii of Φ and Φ_{int} are obtained by

$$\langle \mathbf{r}^2 \rangle \equiv \langle \Phi | \sum_i \mathbf{r}_i^2 | \Phi \rangle, \quad (38)$$

$$\langle \mathbf{r}^2 \rangle_{\text{int}} \equiv \langle \Phi_{\text{int}} | \sum_i (\mathbf{r}_i - \mathbf{X})^2 | \Phi_{\text{int}} \rangle \quad (39)$$

for a single-particle coordinate \mathbf{r}_i , and hence these are related to b as

$$\langle \mathbf{r}^2 \rangle = \langle \mathbf{r}^2 \rangle_{\text{int}} + \frac{3}{2} \frac{b^2}{A}. \quad (40)$$

The CM correction to $\langle \mathbf{r}^2 \rangle$ is small (order $1/A$), so it can be estimated with Φ instead of Φ_{int} :

$$\langle \mathbf{r}^2 \rangle_{\text{int}} \approx \langle \Phi | \sum_i (\mathbf{r}_i - \mathbf{X})^2 | \Phi \rangle. \quad (41)$$

The correction is a combination of the one-body and two-body corrections. Inserting Eq. (41) into Eq. (40), we can determine the size parameter b and then Φ_{int} from Φ .

The proton and neutron density without and with the CM correction are obtained by

$$\rho(\mathbf{r}) = \langle \Phi | \sum_i \delta(\mathbf{r}_i - \mathbf{r}) P_i | \Phi \rangle, \quad (42)$$

$$\rho_{\text{int}}(\mathbf{r}) = \langle \Phi_{\text{int}} | \sum_i \delta(\mathbf{r}_i - \mathbf{X} - \mathbf{r}) P_i | \Phi_{\text{int}} \rangle, \quad (43)$$

where P_i is a projector for proton or neutron. These densities satisfy

$$\rho(\mathbf{r}) = \int d\mathbf{r}' |\Phi_{\text{cm}}(\mathbf{r} - \mathbf{r}')|^2 \rho_{\text{int}}(\mathbf{r}'). \quad (44)$$

Thus, the density ρ_{int} with the CM correction is obtained by unfolding ρ with $|\Phi_{\text{cm}}|^2$.

Instead of the complicated unfolding procedure [50], we can take the following simple prescription. As shown in Eq. (40), the difference between $\langle \mathbf{r}^2 \rangle$ and $\langle \mathbf{r}^2 \rangle_{\text{int}}$ is small, because it is of order $1/A$. This indicates that \mathbf{r} dependence of $\rho_{\text{int}}(\mathbf{r})$ is similar to that of $\rho(\mathbf{r})$. We can then approximate $\rho_{\text{int}}(\mathbf{r})$ by

$$\rho_{\text{int}}(\mathbf{r}) = \frac{1}{\alpha^3} \rho(\mathbf{r}/\alpha) \quad (45)$$

with a scaling factor

$$\alpha = \sqrt{\frac{\langle \mathbf{r}^2 \rangle_{\text{int}}}{\langle \mathbf{r}^2 \rangle}} = \sqrt{1 - \frac{3}{2A} \frac{b^2}{\langle \mathbf{r}^2 \rangle}}, \quad (46)$$

where α has been determined to reproduce $\langle \mathbf{r}^2 \rangle_{\text{int}}$ of Eq. (41). The error of this simple prescription to the unfolding procedure is only 0.1% in σ_R for Ne isotopes, so we use the simple prescription for the density calculated with the mean-field model. The RMS radii, $\sqrt{\langle \mathbf{r}^2 \rangle}$ and $\sqrt{\langle \mathbf{r}^2 \rangle_{\text{int}}}$, without and with the CM correction are estimated with the spherical HF model, and the parameter b is evaluated with Eq. (40) from the RMS radii. For each of Ne isotopes, we use a common b among the HF calculation and the spherical and deformed WS calculations, since the difference of $\sqrt{\langle \mathbf{r}^2 \rangle}$ among these mean-field models are at most 6% and the 6% error to the 1.5% CM correction is negligible.

E. Dynamical deformation and reorientation effects

When the projectile is deformed in the intrinsic frame, the deformation enlarges the radius of the projectile density in the space-fixed frame and eventually enhances the reaction cross section. This static deformation effect has already been included in the DFM by making the AMP. Another effect to be considered is the dynamical deformation effect that is an effect of the rotational motion of the deformed projectile during the scattering. This effect on the reaction cross section is found to be small for intermediate-energy nucleus-nucleus scattering [29]. This was confirmed with the adiabatic approximation to the rotational motion of projectile and the eikonal approximation to the relative motion between the projectile and the target. In this subsection, the effect is investigated with no approximation.

In order to test the dynamical deformation effect, we consider the scattering of ^{30}Ne from ^{12}C at 240 MeV/nucleon and do a coupled-channel calculation between the 0^+ ground state and the first 2^+ state of ^{30}Ne . The projectile density is calculated by the DWS model with the deformation evaluated by the AMD. The coupling potentials in the coupled-channel calculation are obtained by the so-called single-folding model; namely, the nucleon- ^{12}C potential is first evaluated by folding the Melbourne- g matrix interaction with the target density of ^{12}C and the coupling potentials are then obtained

by folding the nucleon- ^{12}C potential with the projectile transition densities.

In the single-channel calculation with no dynamical deformation effect, the resultant reaction cross section is 1469 mb. This result overestimates the corresponding result of the DFM by about 10 %, which is enough to accuracy of the present test. In the coupled-channel calculation with the dynamical deformation effect from the first 2^+ state, the resulting reaction cross section is 1468 mb. Thus the dynamical rotation effect on the reaction cross section is estimated as less than 0.1 %. The reason why the effect is small for intermediate-energy nucleus-nucleus scattering is shown in Ref. [29]. The integrated inelastic cross section to the first 2^+ state is 2.9 mb. This is 0.2 % of σ_R , indicating that $\sigma_I \approx \sigma_R$.

The folding potential U is not spherical in general, when the spin of the projectile is not zero. This effect called the reorientation effect is also tested by the coupled-channel calculation for the scattering of $^{31}\text{Ne}(3/2^-)$ from ^{12}C at 240 MeV/nucleon, where the single-folding model is used. The resultant reaction cross section is 1512 mb, whereas the corresponding cross section is 1515 mb when the non-spherical part of U is switched off. The reorientation effect is 0.2 % and hence negligible for intermediate-energy nucleus-nucleus scattering.

III. RESULTS

A. Reaction cross sections for stable nuclei

We first test the accuracy of the DFM with the Melbourne- g matrix NN interaction for ^{12}C scattering at incident energies (E_{in}) around 240A MeV from stable targets, ^{12}C , ^{20}Ne , ^{23}Na and ^{27}Al . Experimental data on σ_R are available for a ^{12}C target at $E_{\text{in}} = 250.8\text{A}$ MeV and a ^{27}Al target at $E_{\text{in}} = 250.7\text{A}$ MeV [52]. For ^{20}Ne and ^{23}Na targets, σ_I at $E_{\text{in}} = 240\text{A}$ MeV were recently deduced from measured σ_I at around 1 GeV/nucleon [53, 54] with the Glauber model [10].

For these stable nuclei, we take the phenomenological proton-density [55] deduced from the electron scattering by unfolding the finite-size effect of the proton charge in the standard manner [56], and the neutron density is assumed to have the same geometry as the corresponding proton one, since the proton RMS radius deviates from the neutron one only by less than 1% in the Hartree-Fock (HF) calculation.

DFM calculations are done with three types of effective NN interactions: the Love-Franey t -matrix interaction (t_{LF}) [57], the Melbourne- g matrix interaction (g_{MP}) [20] evaluated from the Paris realistic NN interaction [58] and the Melbourne interaction (g_{MB}) [20] constructed from the Bonn-B realistic NN interaction [38].

Table I shows experimental and theoretical reaction cross sections for a ^{12}C target at $E_{\text{in}} = 250.8\text{A}$ MeV and a ^{27}Al target at $E_{\text{in}} = 250.7\text{A}$ MeV. The effective inter-

TABLE I: Reaction cross sections for $^{12}\text{C} + ^{12}\text{C}$ scattering at $E_{\text{in}} = 250.8\text{A}$ MeV and $^{12}\text{C} + ^{27}\text{Al}$ scattering at $E_{\text{in}} = 250.7\text{A}$ MeV. Results of three types of effective nucleon-nucleon interactions are compared with the corresponding data [52]. The cross sections are presented in units of mb.

Target	Exp. [52]	t_{LF} [57]	g_{MP} [20]	g_{MB} [20]
^{12}C	782.0 ± 10.0	917.7	793.1	795.9
^{27}Al	1159.0 ± 14.0	1337.5	1164.9	1185.2

action t_{LF} has no nuclear medium effect. In this case, the theoretical reaction cross sections overestimate the mean values of data [52] by 17% for ^{12}C and by 15% for ^{27}Al . In the cases of g_{MP} and g_{MB} with the medium effect, meanwhile, the overestimation is only a few percent for both ^{12}C and ^{27}Al . The medium effect is thus significant, and an amount of the effect is almost independent of the bare NN interaction taken. As for ^{27}Al , the reaction cross section calculated with g_{MB} agrees with the mean value of data, when the theoretical σ_R is multiplied by the factor $F = 0.978$.

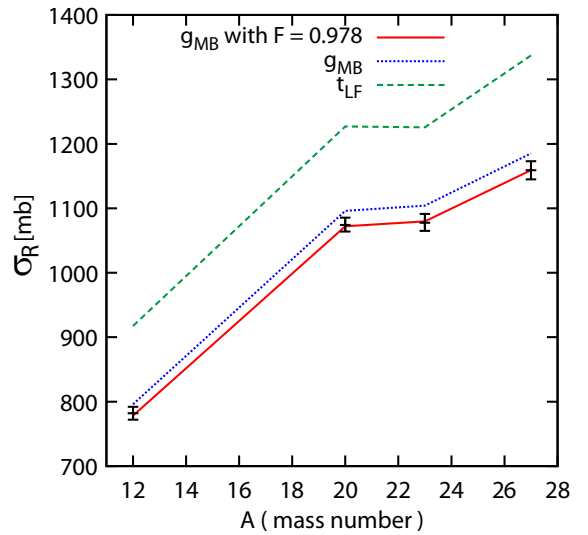


FIG. 2: (Color online) Reaction cross sections for scattering of ^{12}C on stable nuclei from $A = 12$ to 27 . The data at 250.8A MeV for ^{12}C and ^{27}Al are taken from Ref. [52]. The data at 240A MeV for ^{20}Ne and ^{23}Na are deduced from measured σ_I at around 1 GeV/nucleon [53, 54] with the Glauber model [10]. The solid (dotted) line stands for results of the DFM with g_{MB} after (before) the normalization of $F = 0.978$, whereas the dashed line corresponds to results of t_{LF} .

In Fig. 2, σ_R or σ_I is plotted for ^{12}C , ^{20}Ne , ^{23}Na and ^{27}Al targets. The dotted and solid lines represent results of the DFM with g_{MB} before and after the normalization of $F = 0.978$, respectively. Before the normalization pro-

cedure, the dotted line slightly overestimates the mean values of data for $A = 20 - 27$. After the normalization procedure, the solid line agrees with the mean values of data for all the targets. The normalization procedure is thus reliable. The dashed line corresponds to results of t_{LF} with no normalization. The medium effect reduces the theoretical reaction cross sections by about 15% for all the targets.

As for the scattering of Ne isotopes on ^{12}C at 240 MeV/nucleon, we perform the DFM calculation with g_{MB} and the normalization factor F . The DFM calculation with g_{MB} has harmless numerical ambiguity due to the parameterization of g_{MB} ; the imaginary part of the folding potential has a small positive value in the tail region. If the positive imaginary part is cut, it increases the reaction cross section by 2 % for a ^{12}C projectile and by 1 % for Ne isotopes. This cut is used in this paper. If the cut is not taken, F becomes 1.0 and hence the resultant reaction cross sections for Ne isotopes are increased by 1 % from the present results. This numerical ambiguity does not change the conclusion of this paper, since the ambiguity is tiny.

B. AMD analysis for Ne isotopes

Table II shows AMD results for the ground-state properties of Ne isotopes, i.e., the spin-parity (J^π), the one-neutron separation energy S_{-1n} and the values of deformation parameters ($\bar{\beta}, \bar{\gamma}$). The AMD yields the same J^π as the data displayed on the web site [59], although they are not established experimentally for $^{27,29,31}\text{Ne}$. Particularly for ^{31}Ne in the IOI region, the ground state has $J^\pi = 3/2^-$ and small S_{-1n} consistent with the data 0.290 ± 1.640 [60]. For ^{28}Ne corresponding to the boundary of the IOI region, the main component of the ground state is the oblate state with $\bar{\beta} = 0.28$, but it is strongly mixed by the prolate state with $\bar{\beta} = 0.5$. The deformation parameter $\bar{\beta}$ decreases as A increases from 20 to 25 and increases as A increases from 25 to 32. The deformation becomes smallest at $A = 25$.

Figure 3 plots (a) the total binding energy and (b) S_{-1n} as a function of A ; here the data are taken from Refs. [60, 61]. In the HF and HFB calculations, the spherical shape is imposed with the filling approximation, and the nucleus with $A > 30$ are unbound. The Gogny-HF calculations (dotted lines) underestimate the total binding energy systematically. This situation is improved by the Gogny-HFB calculations (dashed lines). The Gogny-AMD calculations (solid lines) yield even better agreement with the data. For S_{-1n} , the Gogny-HF calculations can not reproduce the even-odd difference well, but this problem is improved by the Gogny-HFB calculations. Thus the pairing effect is important for S_{-1n} . The Gogny-AMD calculations almost reproduce the even-odd difference for all Ne isotopes from $A=21$ to 32, but slightly underestimate the experimental even-odd difference. This may indicate that the pairing effect

TABLE II: Ground-state properties of Ne isotopes predicted by the AMD. For ^{28}Ne , the oblate state with $\bar{\beta} = 0.28$ is the main component of the ground state, but it is strongly mixed by the prolate state with $\bar{\beta} = 0.5$.

nuclide	$J^\pi(\text{exp})$	$J^\pi(\text{AMD})$	S_{-1n} [MeV]	$\bar{\beta}$	$\bar{\gamma}$
^{20}Ne	0^+	0^+		0.46	0°
^{21}Ne	$3/2^+$	$3/2^+$	7.111	0.44	0°
^{22}Ne	0^+	0^+	9.779	0.39	0°
^{23}Ne	$5/2^+$	$5/2^+$	6.021	0.32	0°
^{24}Ne	0^+	0^+	8.231	0.25	60°
^{25}Ne	$1/2^+$	$1/2^+$	4.339	0.20	31°
^{26}Ne	0^+	0^+	5.153	0.22	0.1°
^{27}Ne	$(3/2^+)$	$3/2^+$	1.767	0.27	13.6°
^{28}Ne	0^+	0^+	3.123	0.28(0.50)	0°
^{29}Ne	$(3/2^+)$	$1/2^+$	1.321	0.43	0°
^{30}Ne	0^+	0^+	2.025	0.39	0°
^{31}Ne		$3/2^-$	0.248	0.41	0°
^{32}Ne	0^+	0^+	1.012	0.33	0°

is partly included in the Gogny-AMD calculations. The deformation parameter $\bar{\beta}$ is 0.33 for ^{32}Ne and 0.41 for ^{31}Ne . The reduction of $\bar{\beta}$ from 0.41 to 0.33 may come partly from the pairing effect.

Figure 4 represents σ_R for scattering of Ne isotopes on ^{12}C at 240 MeV/nucleon. The AMD calculations (solid line) succeed in reproducing the data [10], while the spherical Gogny-HF calculation (dotted line) under-shoots the data; note that the spherical Gogny-HFB calculation yields the same result as the spherical Gogny-HF calculation within the thickness of line. The nuclei with $A > 30$ are unbound in these spherical calculations. The enhancement from the dotted line to the solid line comes from the deformation of the ground state, since the deformation is a main difference between the two calculations. The AMD results are consistent with all the data except ^{31}Ne . The underestimation of the AMD result for ^{31}Ne comes from the inaccuracy of the AMD density in its tail region.

The tail problem is solved by the following resonating group method [30]. In principle the ground state $\Phi(^{31}\text{Ne}; 3/2_1^-)$ of ^{31}Ne can be expanded in terms of the ground and excited states $\Phi(^{30}\text{Ne}; J_n^\pi)$ of ^{30}Ne . This means that the ground state of ^{31}Ne is described by the $^{30}\text{Ne} + n$ cluster model with the core (^{30}Ne) excitations. The cluster-model calculation can be done with the resonating group method (RGM) in which the ground and excited states of ^{30}Ne are constructed by the AMD:

$$\Phi(^{31}\text{Ne}; 3/2_1^-) = \sum_{nJ\pi} \mathcal{A} \{ \chi_{nlj}(r) Y_{lm}(\hat{r}) \Phi(^{30}\text{Ne}; J_n^\pi) \phi_n \}, \quad (47)$$

where ϕ_n is the intrinsic wave function of last neutron and χ_{nlj} is the relative wave function between the last

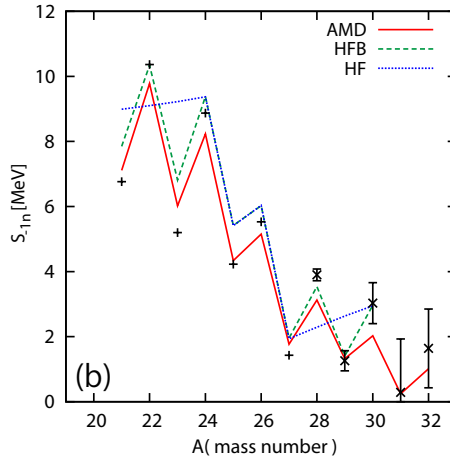
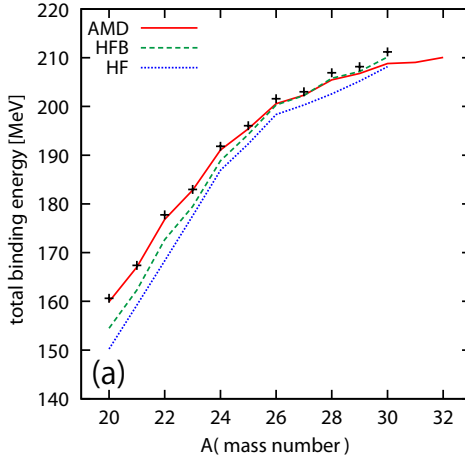


FIG. 3: (Color online) Results of the AMD, the spherical Gogny-HF and the spherical Gogny-HFB calculation for (a) the total binding energy and (b) the one-neutron separation energy of Ne isotopes. The dotted, dashed and solid lines represent results of Gogny-HF, Gogny-HFB and AMD calculations. In the spherical HF calculations, the nuclei with $A > 30$ are unbound. The experimental data are taken from Refs. [59–61].

neutron and the core (^{30}Ne). Here the wave function of ^{30}Ne includes many excited states with positive- and negative-parity below 10 MeV in excitation energy. This AMD+RGM calculation is quite time consuming, but it was done for ^{31}Ne . The tail correction to σ_R is 35 mb.

For a weakly bound system such as ^{31}Ne , furthermore, the projectile breakup effect is not perfectly negligible. This effect is simply estimated by assuming the potential model for the $^{30}\text{Ne}+\text{n}$ system and solving the three-body dynamics of the $^{30}\text{Ne}+\text{n}+^{12}\text{C}$ system with the method of continuum discretized coupled channels (CDCC) [62, 63]. CDCC is an accurate method for treating exclusive reactions such as elastic scattering and elastic-breakup reactions. The theoretical foundation of CDCC is shown in Refs. [64–66]. CDCC succeeded in reproducing data on

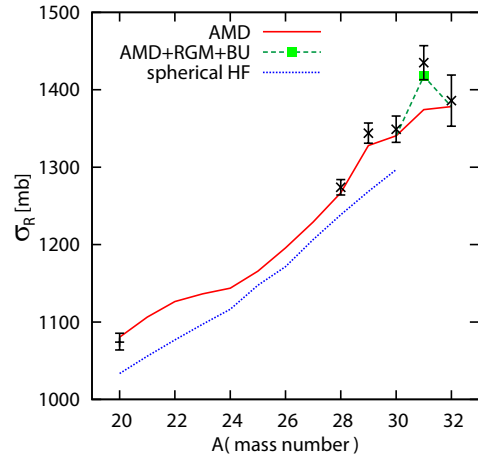


FIG. 4: (Color online) Reaction cross sections for scattering of Ne isotopes on ^{12}C at 240 MeV/nucleon. The solid (dotted) line represents results of the AMD (spherical Gogny-HF) calculations. The dashed line with a closed square is the AMD calculation with the tail and breakup corrections. The experimental data for $A = 28 - 32$ are taken from Ref. [10]. The data for ^{20}Ne is deduced from measured σ_I at around 1 GeV/nucleon [53] with the Glauber model [10].

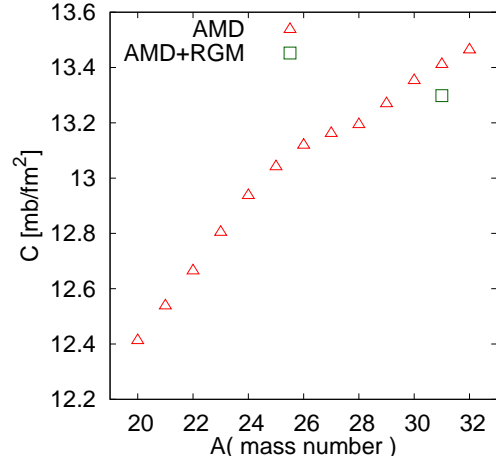


FIG. 5: (Color online) A dependence of the coefficient C . Open triangles show results of the AMD calculations, whereas an open square corresponds to a result of the AMD+RGM calculation for ^{31}Ne . There is a non-negligible difference between the AMD and the AMD+RGM result for ^{31}Ne . Thus, C is slightly reduced, when the density has the halo structure.

the scattering of stable and unstable projectiles [62, 63, 67–80]. Here the interactions between ^{30}Ne and ^{12}C and between n and ^{12}C are constructed with the DFM with the Melbourne g -matrix, and the potential between ^{30}Ne and n is made with the well-depth method; see Refs. [22, 81] for the potential parameters. The correction is 10 mb corresponding to 0.7% of σ_R . In Fig. 4, the dashed line

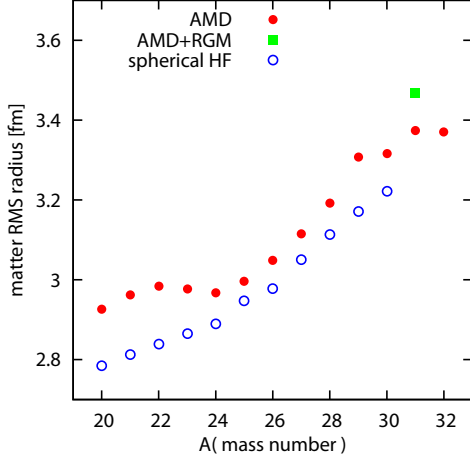


FIG. 6: (Color online) Matter RMS radii of Ne isotopes calculated with the AMD, the AMD+RGM, and the spherical HF model. The closed circle represents results of the AMD, and the closed square denotes a result of the AMD+RGM model for ^{31}Ne . The opened circles are results of the spherical HF calculation.

stands for the AMD result with the tail and breakup corrections for ^{31}Ne . The result is consistent with the data for $^{28-32}\text{Ne}$.

The reaction cross section σ_R is sensitive to the RMS radii, $\sqrt{\langle \mathbf{r}^2 \rangle_P}$ and $\sqrt{\langle \mathbf{r}^2 \rangle_T}$, of projectile and target. Actually, the DFM calculation for $^{20-32}\text{Ne}$ projectiles shows that

$$\sigma_R = C\pi \left[\sqrt{\langle \mathbf{r}^2 \rangle_P} + \sqrt{\langle \mathbf{r}^2 \rangle_T} \right]^2, \quad (48)$$

where C is a slowly varying function of A around $C = 12.4 \sim 13.5$ [mb/fm 2], as shown in Fig. 5. Now it is assumed that the projectile density has a deformed well shape. If the volume conservation is imposed with the general shape in Eq. (30), the matter squared radius $\langle \mathbf{r}^2 \rangle_P$ of projectile is described by

$$\langle \mathbf{r}^2 \rangle_P = \langle \mathbf{r}^2 \rangle_0 \left[1 + \frac{5}{4\pi} \sum_{\lambda\mu} |\alpha_{\lambda\mu}|^2 \right] \quad (49)$$

$$= \langle \mathbf{r}^2 \rangle_0 \left[1 + \frac{5}{4\pi} (\beta_2^2 + \beta_4^2 + \dots) \right] \quad (50)$$

up to the second order in the deformation parameters $\{\alpha_{\lambda\mu}\}$, where $\langle \mathbf{r}^2 \rangle_0$ is the matter squared radius in the spherical limit. The triaxial parameter γ does not appear in Eq. (50). This means that the triaxial deformation little affect the RMS radius and then σ_R ; it has been confirmed by utilizing the Woods-Saxon model in place of the AMD model, in which the triaxial parameter $\bar{\gamma}$ is optimized and cannot be changed artificially. For ^{27}Ne , we varied the γ parameter from 0° to 60° with fixing $\beta_2 = 0.273$ ($\beta_4 = 0$) corresponding to the $\bar{\beta} = 0.27$ predicted by the AMD model, but the resultant reaction

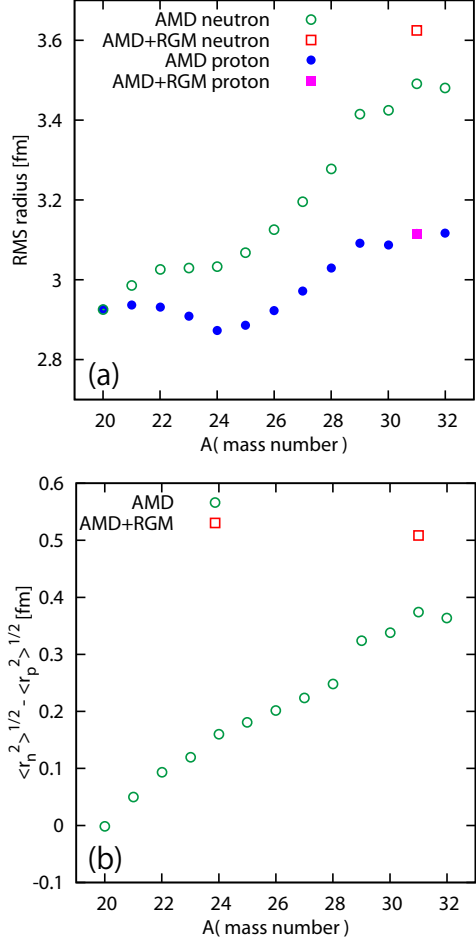


FIG. 7: (Color online) Neutron and proton RMS radii of Ne isotopes calculated with the AMD and the AMD+RGM model. In panel (a), the closed (opened) circle represents the proton (neutron) RMS radius calculated with the AMD and the closed (opened) square denotes a result of the AMD+RGM calculation for proton (neutron) of ^{31}Ne ; note that the AMD+RGM result agrees with the AMD result for proton RMS radius. Panel (b) shows the difference between neutron and proton RMS radii. The open circle (square) stands for the AMD (AMD+RGM) result.

cross section changes only by 0.2%. Figure 6 shows the RMS radii of the spherical-HF, AMD, AMD+RGM calculations. The differences among three calculations for the RMS radii are similar to those for σ_R shown in Fig. 4. The difference between the AMD and AMD+RGM calculations for the RMS radius of ^{31}Ne is appreciable, indicating that the tail correction is significant for this very-weakly bound system.

Finally we compare the neutron RMS radius $\sqrt{\langle \mathbf{r}_n^2 \rangle}$ with the proton one $\sqrt{\langle \mathbf{r}_p^2 \rangle}$ in order to see the isovector components of the Ne-isotope densities. Figure 7 shows A -dependence of $\sqrt{\langle \mathbf{r}_n^2 \rangle}$ and $\sqrt{\langle \mathbf{r}_p^2 \rangle}$ for Ne isotopes. In

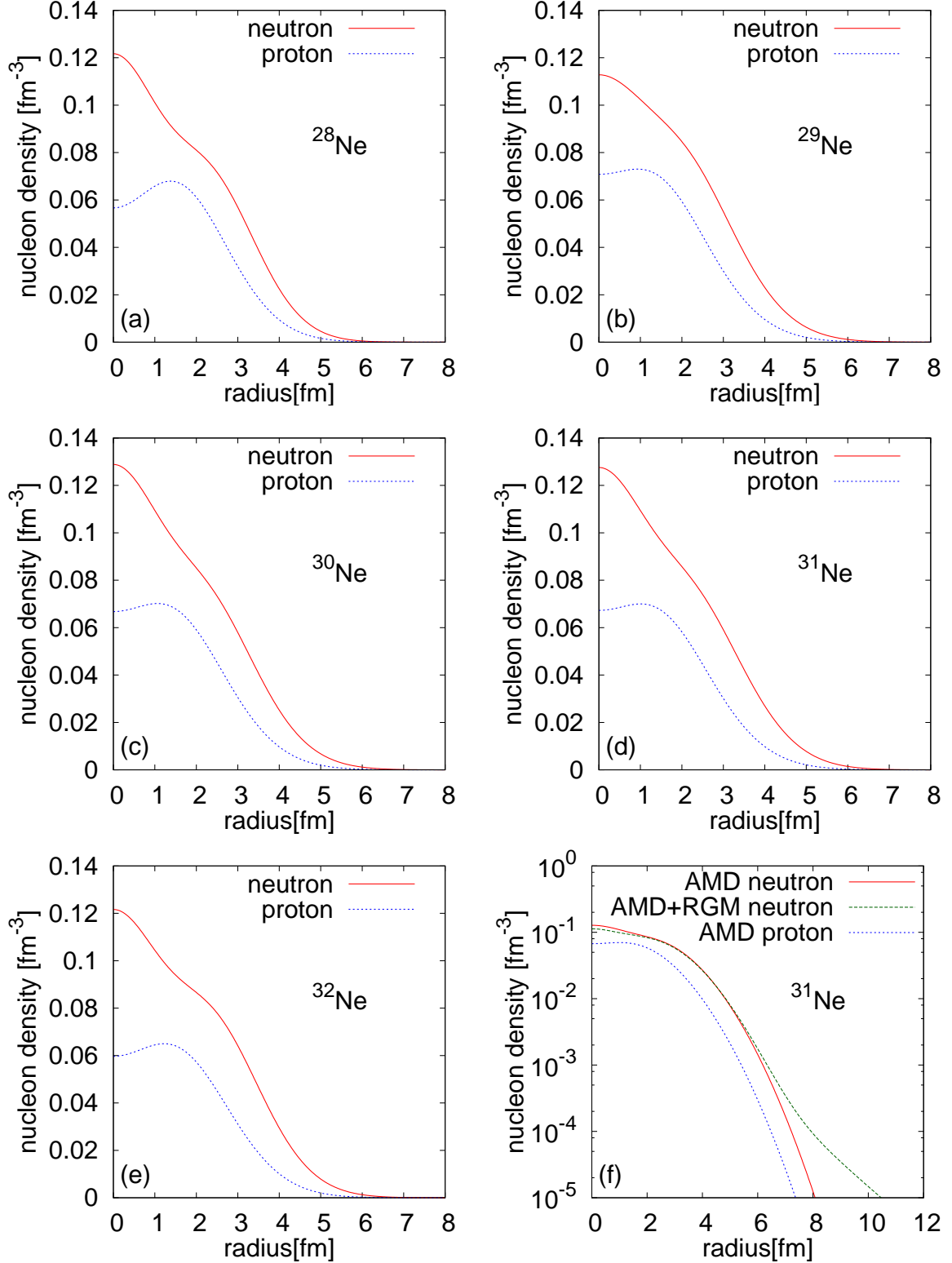


FIG. 8: (Color online) Neutron and proton density profiles for (a) ^{28}Ne , (b) ^{29}Ne , (c) ^{30}Ne , (d) ^{31}Ne and (e) ^{32}Ne on a linear scale and (f) ^{31}Ne on a logarithmic scale. In panels (a)-(f), the solid (dotted) line presents the neutron (proton) density profile calculated with the AMD method, whereas the dashed line in panel (f) is the neutron density profile calculated with the AMD+RGM method.

panel (a), the neutron and proton RMS radii increase with A , when $A \geq 24$. For $A = 20 - 24$, the proton RMS radii have a bump. This implies that at $A = 20 - 22$ the proton-neutron correlation is strong and hence the alpha-clustering grows. Panel (b) shows the difference $\sqrt{\langle r_n^2 \rangle} - \sqrt{\langle r_p^2 \rangle}$ as a function of A . The difference also goes up as A increases. There is a sizable jump between $A = 28$ and 29 , since the deformation $\bar{\beta}$ is around 0.25 at $A = 24 - 28$ but around 0.4 at $A = 29 - 32$. As a result of this gap, the radius difference is around 0.35 fm, indicating that Ne isotopes are either skin or skin-like nuclei for $A = 29, 30, 32$. For ^{31}Ne , the radius difference calculated with the AMD+RGM method is about 0.5 fm that is significantly bigger than 0.35 fm. This implies that ^{31}Ne is a halo nucleus. These interpretations are more obvious through the neutron and proton density profiles shown in Fig. 8. Panels (a), (b), (c), (d), and (e) show the density profiles for $^{28-32}\text{Ne}$, respectively. $^{29,30,32}\text{Ne}$ have the neutron-skin structure. In panel (f), the density profiles for ^{31}Ne is plotted on a logarithmic scale. The neutron density (dashed line) calculated with the AMD+RGM method has a long-range tail, indicating that ^{31}Ne has the halo structure.

C. Woods-Saxon mean-field model

In this subsection, the results of the Woods-Saxon mean-field model are investigated. First of all, in order to see that the parameter set of the Woods-Saxon potential is reasonable, the spherical case is studied. Figure 9 shows the reaction cross sections for Ne isotopes calculated with the spherical Woods-Saxon (SWS) model (neglecting the pairing correlation) and the spherical Gogny-HF method. The SWS model (dotted line) well simulates results of the spherical Gogny-HF calculation (solid line). This means that the SWS model yields almost the same matter radius as the spherical Gogny-HF calculation. The SWS model with the present parameter set proposed by R. Wyss [31] is thus a handy way of simulating the spherical Gogny-HF calculation.

Figure 10 shows the neutron Nilsson diagram for ^{30}Ne calculated with the DWS model. It is emphasized that the relatively large shell gap with $N = 20$ is observed at the spherical shape ($\beta_2 = 0$). Comparing this figure with the Nilsson diagram calculated with the AMD model in Fig. 2 of Ref. [27], one can see that the Nilsson diagram of the DWS model is close to that of the AMD model. In both the models (AMD and DWS), the $[2,0,0,1/2]$ and the $[3,3,0,1/2]$ orbit in terms of the Nilsson asymptotic quantum numbers $[N,n_3,\Lambda,\Omega]$ cross each other at $\beta_2 \approx 0.4$, although the single-particle energy at the crossing point is -3 MeV in the AMD model and -4 MeV in the DWS model. It is well-known that the occupation of this down-sloping orbit $[3,3,0,1/2]$ derives the system to deform near $N \approx 20$.

Next, the results of the deformed Woods-Saxon (DWS)

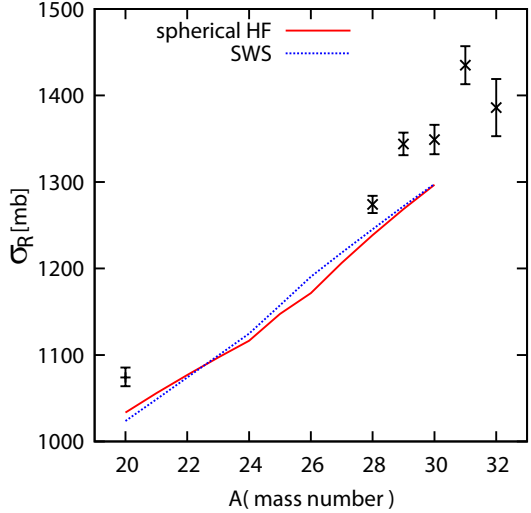


FIG. 9: (Color online) Reaction cross sections calculated for Ne isotopes calculated with the SWS model and the Gogny-HF method. The spherical shape is imposed for both the calculations. The dotted line represents results of the SWS model, while the solid line corresponds to the spherical Gogny-HF results. The nucleus with $A > 30$ are unbound. The experimental data are taken from Ref. [10].

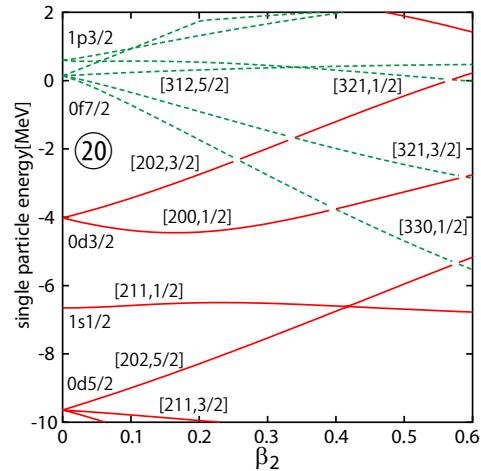


FIG. 10: (Color online) The neutron Nilsson diagram for ^{30}Ne in the deformed WS model, where the other parameters are fixed to $\beta_4 = \gamma = 0$. The solid (dashed) lines correspond to the positive (negative) parity orbits. The Nilsson asymptotic quantum numbers $[N,n_3,\Lambda,\Omega]$ are attached. The number 20 stands for a neutron magic number in the spherical limit.

model with deformation obtained by the microscopic-macroscopic (Strutinsky) method are discussed. The pairing correlation is included within the Kruppa-BCS approximation, which strongly affects the resultant deformations. Two cases of the pairing strengths determined by the smooth pairing gap $\tilde{\Delta} = 12/\sqrt{A}$ or $4/\sqrt{A}$ MeV are

TABLE III: Deformation parameters (β_2, β_4) and the pairing gaps Δ_n and Δ_p obtained by the Strutinsky calculation with $\tilde{\Delta} = 12/\sqrt{A}$ MeV. The nucleus ^{31}Ne is unbound and * is attached.

nuclide	β_2	β_4	Δ_n [MeV]	Δ_p [MeV]
^{20}Ne	0.000	0.000	2.897	2.848
^{21}Ne	0.310	0.048	0.000	2.290
^{22}Ne	0.000	0.000	2.801	2.826
^{23}Ne	0.200	0.011	0.889	2.596
^{24}Ne	0.000	0.000	2.337	2.865
^{25}Ne	0.000	0.000	0.000	2.849
^{26}Ne	0.000	0.000	2.157	2.826
^{27}Ne	-0.065	-0.002	0.989	2.783
^{28}Ne	0.000	0.000	2.345	2.783
^{29}Ne	-0.048	-0.001	1.391	2.748
^{30}Ne	0.000	0.000	2.286	2.734
^{31}Ne	0.101*	0.022*	1.618	2.623
^{32}Ne	0.000	0.000	2.416	2.674

considered; $\tilde{\Delta} = 12/\sqrt{A}$ MeV is often used as a typical value for medium-heavy nuclei, while $\tilde{\Delta} = 4/\sqrt{A}$ MeV is used to simulate the weak pairing case. The smooth pairing gap $\tilde{\Delta}$ is usually supposed to correspond to the even-odd mass difference. However, in the light mass nuclei, like the Ne isotopes considered in the present work, the even-odd mass differences contain considerable amount of the shell effect of deformed mean-field, and the weaker pairing correlations are suggested [82]. The small value $\tilde{\Delta} = 4/\sqrt{A}$ MeV is chosen in accordance with it. In Tables III and IV, the results of the deformation parameters (β_2, β_4) and the neutron and proton pairing gaps Δ_n and Δ_p are summarized; all nuclei are calculated to be axially symmetric in their ground states. If the standard pairing is used, all even-even isotopes turn out to be spherical, which contradicts the result of the AMD calculation. Even with weaker pairing, $^{25,26,28,30}\text{Ne}$ are calculated to be spherical; this is because of the relatively large $N = 20$ shell gap (see Fig. 10), which is in contrast to the prediction using the tensor force in Ref. [83].

In order to check the consistency of the DWS model, we compare the obtained deformations with the systematic Gogny D1S HFB calculations [84], the results of which are available on the web site [85]. Those results are also axially symmetric in Ne isotopes, and the (β_2, β_4) deformation parameters are extracted in such a way that $\langle r^2 Y_{20} \rangle_{\text{uni}} / \langle r^2 \rangle_{\text{uni}}$ and $\langle r^4 Y_{40} \rangle_{\text{uni}} / \langle r^2 \rangle_{\text{uni}}^2$ calculated with the uniform density in Eq. (32) reproduce the corresponding values of Gogny D1S HFB calculations tabulated in Ref. [85]. The resultant (β_2, β_4) are listed in Table V. It can be seen that (β_2, β_4) calculated with the weaker pairing in Table IV well corresponds to those of the deformed Gogny D1S HFB results. This result may suggest that the monopole pairing strength weaker than the standard

TABLE IV: The same as Table III but with $\tilde{\Delta} = 4/\sqrt{A}$ MeV.

nuclide	β_2	β_4	Δ_n [MeV]	Δ_p [MeV]
^{20}Ne	0.336	0.111	0.000	0.000
^{21}Ne	0.349	0.079	0.000	0.000
^{22}Ne	0.362	0.051	0.000	0.000
^{23}Ne	0.291	0.052	0.000	0.000
^{24}Ne	0.186	0.018	0.000	1.434
^{25}Ne	0.000	0.000	0.000	1.657
^{26}Ne	0.000	0.000	0.000	1.654
^{27}Ne	0.122	-0.001	0.000	1.471
^{28}Ne	0.001	0.000	0.966	1.638
^{29}Ne	0.067	-0.001	0.000	1.572
^{30}Ne	0.000	0.000	0.000	1.611
^{31}Ne	0.291*	0.106*	0.000	0.000
^{32}Ne	0.278	0.098	0.922	0.000

TABLE V: Deformation parameters (β_2, β_4) extracted from the results of deformed Gogny-D1S HFB calculations of Refs. [84, 85]. The nucleus ^{31}Ne is unbound and no data are available.

nuclide	β_2	β_4
^{20}Ne	0.325	0.108
^{21}Ne	0.370	0.085
^{22}Ne	0.355	0.016
^{23}Ne	0.234	0.011
^{24}Ne	0.179	0.011
^{25}Ne	-0.047	0.001
^{26}Ne	-0.002	0.000
^{27}Ne	-0.073	-0.005
^{28}Ne	-0.006	0.000
^{29}Ne	-0.060	-0.003
^{30}Ne	-0.002	0.000
^{31}Ne	—	—
^{32}Ne	0.246	0.096

one is more appropriate in light nuclei in accordance with the analysis in Ref. [82].

The calculated binding energies and one-neutron separation energies in the DWS model are compared with experimental data in Fig. 11. The binding energies are slightly overestimated for unstable isotopes $^{27-30}\text{Ne}$, which is mainly due to the liquid drop energy [45] employed in the present work. As for the one-neutron separation energies, S_{-1n} , the calculations with the standard pairing strength with $\tilde{\Delta} = 12/\sqrt{A}$ MeV nicely reproduce the experimental data, although the weaker pairing with $\tilde{\Delta} = 4/\sqrt{A}$ MeV may yield slightly better agreement for $^{30-32}\text{Ne}$. Similar agreement is seen in the AMD, but the

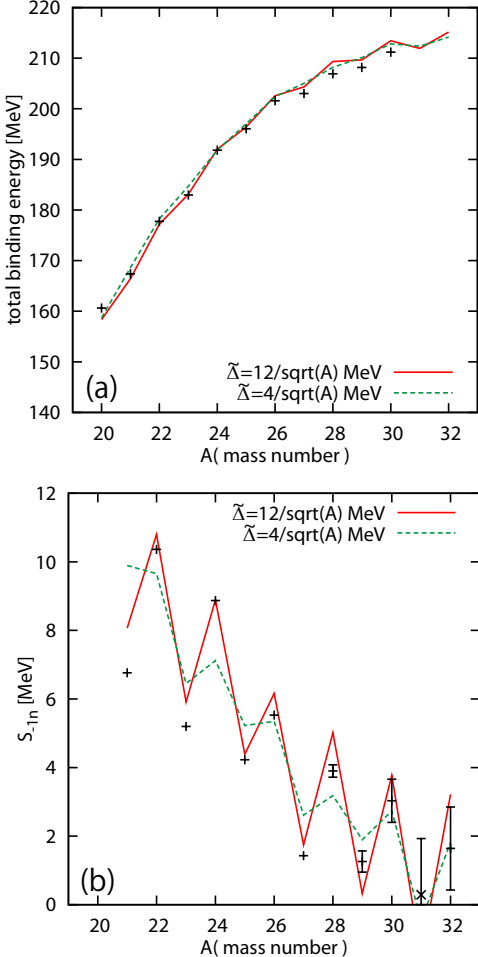


FIG. 11: (Color online) Results of the DWS model including the pairing correlation with $\tilde{\Delta} = 12/\sqrt{A}$ or $4/\sqrt{A}$ MeV for (a) the total binding energy and (b) the one-neutron separation energy S_{1n} of Ne isotopes. The solid line is a result of $\tilde{\Delta} = 12/\sqrt{A}$ MeV and the dashed line of $\tilde{\Delta} = 4/\sqrt{A}$ MeV.

predicted deformations of Ne isotopes in the two models are very different; those in the AMD are larger particularly in unstable isotopes $^{28-32}\text{Ne}$. This is because the binding energy reflects many structural effects. The binding energy is thus not a good indicator of deformation.

Of course, the well-known indicator of nuclear deformation is the rotational spectra and the $E2$ transition probabilities. They are, however, difficult to measure in unstable nuclei. As already discussed in the previous subsection, the reaction cross section σ_R can be utilized instead. Figure 12 shows σ_R for Ne isotopes calculated with the DWS model. The deformation parameters and pairing gaps are calculated either with $\tilde{\Delta} = 12/\sqrt{A}$ or $4/\sqrt{A}$ MeV, and listed in Table III or IV. A result of the DWS model with the deformations calculated with the deformed Gogny-D1S HFB method [84, 85] (Table V) is

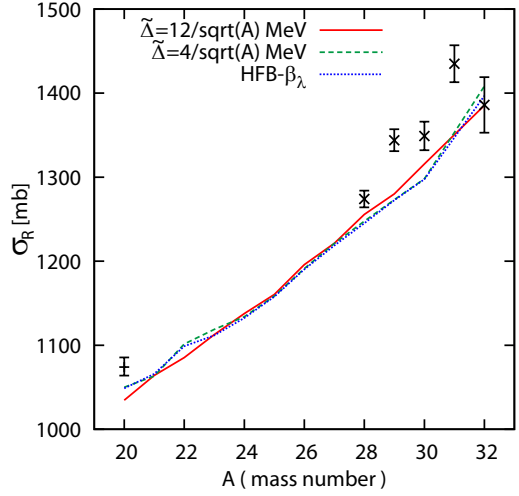


FIG. 12: (Color online) The reaction cross sections for Ne isotopes calculated with the DWS model with some sets of deformation parameters. The solid and dashed lines represent results of the Strutinsky method with $\tilde{\Delta} = 12/\sqrt{A}$ and $4/\sqrt{A}$ MeV. In the dotted line, the deformation is determined by the deformed Gogny-D1S HFB calculation, for which the pairing correlation is neglected. The experimental data are taken from Ref. [10].

also included as a dotted line. Comparing with the deformation parameters obtained with the AMD (Table II), the used value of deformation parameters are zero or small around ^{30}Ne since the neutron number $N = 20$ is a spherical magic number. As a consequence of this, the reaction cross sections based on both the microscopic-macroscopic (Strutinsky) and the deformed Gogny-D1S HFB methods underestimate the experimental data for $^{28-31}\text{Ne}$. Note that the effect of finite pairing gap alone is small if deformation is fixed as it is shown in the next subsection (see Fig. 16).

The reason why the AMD calculation gives large deformations in the IOI region is that the optimum deformation is searched after the angular momentum projection (note that the same Gogny D1S force is used in the HFB calculation of Refs. [84, 85]). It is known that the potential energy surface as a function of quadrupole deformation is rather shallow for nuclei in the IOI region. In such a case, the energy gain of the AMP at large deformation can easily change the equilibrium deformation, see e.g. Ref. [26] for Ne isotopes. The angular momentum projection is thus important for the IOI region to obtain large deformations.

D. Woods-Saxon model with AMD deformation

In the previous subsection, it has been shown that the microscopic-macroscopic method with the DWS model as well as the deformed Gogny-D1S HFB approach (with-

TABLE VI: Deformation parameter β_2 and γ deduced from the AMD intrinsic density. Those with higher multipoles $\lambda > 2$ are not included. The Nilsson asymptotic quantum numbers of last neutron are included as the last column for axially symmetric cases.

nuclide	$\bar{\beta}$	$\bar{\gamma}$	β_2	γ	[N, n_3, Λ, Ω] for last-n
^{20}Ne	0.46	0°	0.479	0°	[2,2,0,1/2]
^{21}Ne	0.44	0°	0.456	0°	[2,1,1,3/2]
^{22}Ne	0.39	0°	0.400	0°	[2,1,1,3/2]
^{23}Ne	0.32	0°	0.325	0°	[2,0,2,5/2]
^{24}Ne	0.25	60°	0.258	60°	[2,0,0,1/2]
^{25}Ne	0.20	31°	0.202	31.5°	
^{26}Ne	0.22	0.1°	0.221	0°	[2,1,1,1/2]
^{27}Ne	0.27	13.6°	0.273	14.1°	
^{28}Ne	0.50	0°	0.526	0°	[3,3,0,1/2]
	0.28	60°	0.291	60°	[2,1,1,3/2]
^{29}Ne	0.43	0°	0.445	0°	[2,0,0,1/2]
^{30}Ne	0.39	0°	0.400	0°	[2,0,0,1/2]
^{31}Ne	0.41	0°	0.422	0°	[3,2,1,3/2]
^{32}Ne	0.33	0°	0.335	0°	[2,0,2,3/2]

out the AMP) do not give expected large deformations in the IOI region. Therefore, we employ, throughout in this subsection, the deformations obtained by the AMD in the DWS model and compare the results with the AMD calculations and experimental data. In most of this subsection, the pairing correlation is neglected; its effect is discussed at the end.

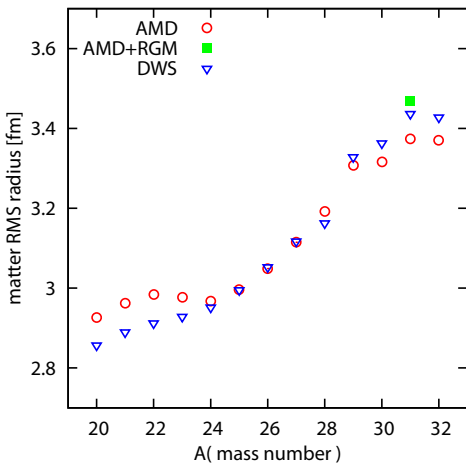


FIG. 13: (Color online) Matter RMS radii of Ne isotopes calculated with the DWS, AMD and AMD+RGM models. The opened circles represent results of the AMD model, and the closed square denotes a result of the AMD+RGM model for ^{31}Ne . The opened inverted triangles are results of the deformed Woods-Saxon calculation.

Table VI lists up the deformation parameters β_2 and γ deduced from the corresponding AMD values $\bar{\beta}$ and $\bar{\gamma}$ and used in the following DWS calculations. In Fig. 13, the matter RMS radius calculated with the DWS model is compared with those of the AMD and AMD+RGM calculations. The DWS model well reproduces the matter RMS radii of the AMD calculation for $^{24-29}\text{Ne}$ in which S_{-1n} is large. For $^{30-32}\text{Ne}$ in which S_{-1n} is small, the matter RMS radii of the AMD calculation are slightly smaller than those of the DWS model. The deviation may come from the fact that the AMD density is inaccurate in its tail region, since the DWS model almost reproduces the matter RMS radius of the AMD+RGM calculation for ^{31}Ne . For $^{20-23}\text{Ne}$, the matter RMS radii of the AMD calculation are larger than those of the DWS model. This may imply that the α clustering is well developed in the AMD calculation and the different type of deformation from those included in the present Woods-Saxon model, e.g., the octupole deformation ($\alpha_{3\mu}$), may be important for $^{20-23}\text{Ne}$.

The nucleon density distributions are plotted in Fig. 14 for ^{24}Ne and ^{31}Ne . The AMD densities (dotted curves) decrease with increasing r more rapidly than the densities (dashed curves) of the DWS model. The deviation between the two densities at large r is rather small for ^{24}Ne where S_{-1n} is large. The deviation is, however, enlarged for ^{31}Ne in which S_{-1n} is small. The AMD density is thus inaccurate at large r particularly for ^{31}Ne . A tail-correction to the AMD density can be made by the AMD+RGM calculation. The density (solid curve) has actually a long-range tail and consequently becomes close to that of the DWS model. As an important result, the density of the DWS model almost agrees with that of the AMD+RGM calculation for ^{31}Ne with $\beta_2 = 0.422$. This result indicates that the DWS model with the AMD deformation is considered to be a handy way of making a tail correction to the AMD density.

In Fig. 15, the reaction cross sections are calculated for Ne isotopes with the DWS, AMD and AMD+RGM models. The differences among the three calculations are similar to the corresponding differences for the matter RMS radii shown in Fig. 13, as expected. Note that the result of the DWS model nearly agrees with that of the AMD+RGM model. As an important result, the reaction cross sections calculated with the DWS model are consistent with the experimental data [10].

Finally, the effect of pairing correlation is investigated for the deformations given by the AMD model. Two cases of the pairing strengths given by the standard value $\tilde{\Delta} = 12/\sqrt{A}$ MeV and the weaker value $\tilde{\Delta} = 4/\sqrt{A}$ MeV are considered as in the previous subsection, and the result is shown in Fig. 16. With the AMD deformations the even-odd effect on the separation energies S_{-1n} for $^{29-32}\text{Ne}$ is too much enhanced if the standard pairing strength is used, while a better fitting is obtained with the weaker pairing strength, as is shown in Fig. 16(a). In Fig. 16(b), the reaction cross sections for Ne isotopes are evaluated by the DWS calculations with different pairing

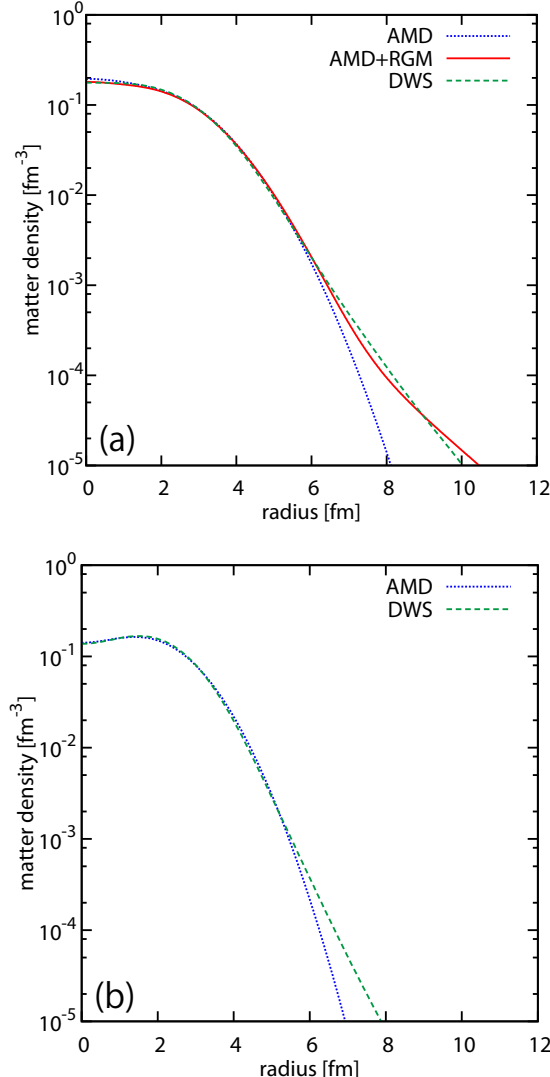


FIG. 14: (Color online) Density distributions of (a) ^{31}Ne and (b) ^{24}Ne . The dotted line represents a result of the AMD model, whereas the dashed line corresponds to a result of the DWS model. The solid line is a result of the AMD+RGM model.

strengths. The reaction cross sections are enhanced a bit by the pairing effect, but its effect is small even with the standard pairing strength.

For weakly bound systems, it is speculated that the pairing correlation leads to an extra binding of halo orbit and makes the nuclear radius shrink; it is called the “pairing anti-halo” effect [86, 87]. Our Kruppa-BCS method can produce the anti-halo like effect [48], but a reduction due to the pairing effect is not observed in the present calculations. Possible reasons may be the large deformations, which tend to prevent the anti-halo effect, and that the binding of the last neutron orbit is not weak enough. As a future work, the deformed HFB calculation is highly expected to answer whether the “pairing anti-halo” effect

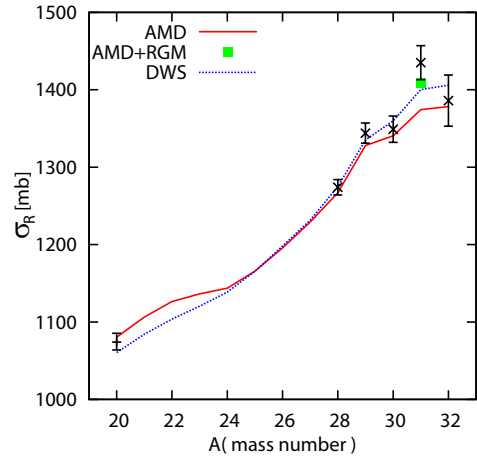


FIG. 15: (Color online) Reaction cross sections for Ne isotopes calculated with the DWS, AMD and AMD+RGM models. The dotted line represents results of the DWS model, while the solid line corresponds to the AMD results. The closed square represents a result of the AMD+RGM calculation without breakup contribution. The experimental data are taken from Ref. [10].

really occurs and reflects the reaction cross section.

In the DWS model that corresponds to the AMD model with the tail correction, σ_R for ^{32}Ne is slightly larger than that for ^{31}Ne as shown in Fig. 15, but the RMS radius for ^{32}Ne is smaller than that for ^{31}Ne as presented in Fig. 13. The reduction of the RMS radius comes from that of β_2 . It is interesting to consider what causes the reduction of β_2 . This is another interesting future subject related to the “pairing anti-halo” effect mentioned above.

IV. SUMMARY

We determined deformations of $^{20-32}\text{Ne}$ with the fully-microscopic AMD model that has no adjustable parameter. The quadrupole deformation parameter determined is around 0.4 in the IOI region and ^{31}Ne is then a halo nuclei with large deformation.

We have also performed the microscopic-macroscopic (Strutinsky) calculations with the Woods-Saxon potential, and found that the obtained deformations are too small, which is consistent with the deformed HFB calculations without the AMP in this region.

As a reaction model, we used the DFM with the Melbourne g -matrix. The microscopic reaction model yields good agreement with the measured σ_R for $^{20,28-32}\text{Ne}$, if the projectile density is constructed either (I) by the AMP-AMD calculation with the Gogny D1S interaction or (II) by the Woods-Saxon mean-field model with the deformation obtained by the AMP-AMD calculation. Method I has no adjustable parameter, but the tail of the density is inaccurate. We then made a tail correction

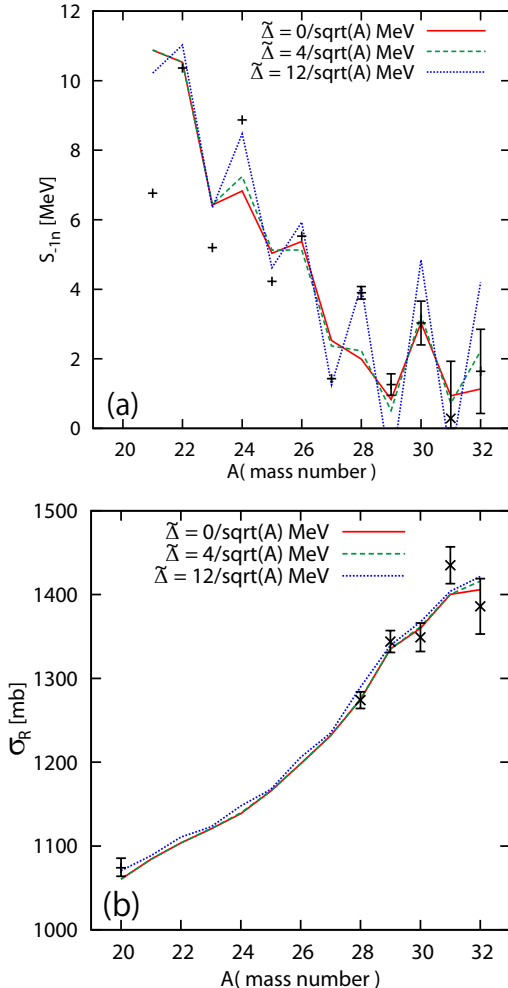


FIG. 16: (Color online) The pairing effect on (a) the one-neutron separation energy S_{-1n} and (b) the reaction cross sections σ_R for Ne isotopes. The solid line is a result of the DWS model without pairing correction and the dashed (dotted) lines stand for a result of the DWS model including the pairing correlation with $\tilde{\Delta} = 4/\sqrt{A}$ ($12/\sqrt{A}$) MeV. The experimental data are taken from Ref. [60, 61] in panel (a) and from Ref. [10] in panel (b).

to the AMD density for ^{31}Ne by using the AMD+RGM method. Method II provides the nucleon density with the proper asymptotic form, but a parameter set of the Woods-Saxon potential should be carefully chosen. The parameter set recently proposed by R. Wyss [31] is shown to be very successful: Method II yields almost the same σ_R as the AMD+RGM method. This means that Method II is a handy way of simulating results of Method I with the tail correction.

The two types of DFM well reproduce the measured σ_R for $^{20,28-32}\text{Ne}$. Deformations of $^{28-32}\text{Ne}$ were definitely determined through this analysis. This analysis also yields a reasonable prediction for deformations of $^{21-27}\text{Ne}$. We also showed that the AMP is essential to obtain the large deformations required for reproducing the measured σ_R for $^{28-32}\text{Ne}$ but that the effect of the BCS-type pairing correlation is small there.

Acknowledgements

The authors thank M. Takechi for providing the numerical data and H. Sakurai, M. Fukuda, and D. Baye for useful discussions. This work is supported in part by Grant-in-Aid for Scientific Research (C) No. 22540285 and 22740169 from Japan Society for the Promotion of Science. The numerical calculations of this work were performed on the computing system in Research Institute for Information Technology of Kyushu University.

-
- [1] E. K. Warburton, J. A. Becker, and B. A. Brown, Phys. Rev. C **41**, 1147 (1990).
 - [2] T. Motobayashi *et al.*, Phys. Lett. B **346**, 9 (1995).
 - [3] E. Caurier, F. Nowacki, A. Poves, J. Retamosa, Phys. Rev. C **58**, 2033 (1998).
 - [4] Y. Utsuno, T. Otsuka, T. Mizusaki, M. Honma, Phys. Rev. C **60**, 054315 (1999).
 - [5] H. Iwasaki *et al.*, Phys. Lett. B **522**, 227 (2001).
 - [6] Y. Yanagisawa *et al.*, Phys. Lett. B **566**, 84 (2003).
 - [7] I. Tanihata, *et al.*, Phys. Lett. B **289**, 261 (1992).
I. Tanihata, J. Phys. G **22**, 157 (1996).
 - [8] A. S. Jensen, *et al.*, Rev. Mod. Phys. **76**, 215 (2004).
 - [9] B. Jonson, Phys. Rep. **389**, 1 (2004).
 - [10] M. Takechi *et al.*, Nucl. Phys. A**834**, 412c (2010).
 - [11] T. Nakamura, *et al.*, Phys. Rev. Lett. **103**, 262501 (2009).
 - [12] A. Gade, *et al.*, Phys. Rev. C **77**, 044306 (2008).
 - [13] G. Bertsch, J. Borysowicz, M. McManus, and W.G. Love, Nucl. Phys. A**284**, 399(1977).
 - [14] J.-P. Jeukenne, A. Lejeune and C. Mahaux, Phys. Rev. C**16**, 80 (1977); *ibid.* Phys. Rep. **25**, 83 (1976).
 - [15] F.A. Brieva and J.R. Rook, Nucl. Phys. A**291**, 299 (1977); *ibid.* 291, 317 (1977); *ibid.* 297, 206 (1978).
 - [16] G. R. Satchler, Phys. Rep. **55**, 183-254 (1979).
 - [17] G. R. Satchler, "Direct Nuclear Reactions", Oxford University Press, (1983).
 - [18] N. Yamaguchi, S. Nagata and T. Matsuda, Prog. Theor.

- Phys. **70**, 459 (1983); N. Yamaguchi, S. Nagata and J. Michiyama, Prog. Theor. Phys. **76**, 1289 (1986).
- [19] L. Rikus, K. Nakano and H. V. von Geramb, Nucl. Phys. **A414**, 413 (1984); L. Rikus and H.V. von Geramb, Nucl. Phys. **A426**, 496 (1984).
- [20] K. Amos, P. J. Dortmans, H. V. von Geramb, S. Karatagliidis, and J. Raynal, in *Advances in Nuclear Physics*, edited by J. W. Negele and E. Vogt(Plenum, New York, 2000) Vol. 25, p. 275.
- [21] T. Furumoto, Y. Sakuragi, and Y. Yamamoto, Phys. Rev. C**78**, 044610 (2008); *ibid.*, C**79**, 011601(R) (2009); *ibid.*, C**80**, 044614 (2009).
- [22] M. Yahiro, K. Ogata, and K. Minomo, Prog. Theor. Phys. **126**, 167(2011).
- [23] J. Terasaki, H. Flocard, P.-H. Heenen, and P. Bonche, Nucl. Phys. A **621**, 706 (1997).
- [24] R. Rodríguez-Guzmán, J.L. Egido, and L.M. Robledo, Nucl. Phys. A **709**, 201 (2002).
- [25] M. Yamagami and Nguyen Van Giai, Phys. Rev. C **69**, 034301 (2004).
- [26] R.R. Rodríguez-Guzmán, J.L. Egido, and L.M. Robledo, Eur. Phys. J. A **17**, 37 (2003).
- [27] M. Kimura and H. Horiuchi, Prog. Theor. Phys. **111**, 841 (2004).
- [28] M. Kimura, Phys. Rev. C**75**, 041302 (2007).
- [29] K. Minomo, T. Sumi, M. Kimura, K. Ogata, Y. R. Shimizu, and M. Yahiro, Phys. Rev. C **84**, 034602 (2011).
- [30] K. Minomo, T. Sumi, M. Kimura, K. Ogata, Y. R. Shimizu and M. Yahiro, arXiv:1110.3867 [nucl-th].
- [31] R. Wyss, private communication(2005).
- [32] K. M. Watson, Phys. Rev. **89**, 115 (1953).
- [33] A. K. Kerman, H. McManus, and A. M. Thaler, Ann. Phys.(N.Y.) **8**, **51** (1959).
- [34] M. Yahiro, K. Minomo, K. Ogata, and M. Kawai, Prog. Theor. Phys. **120**, 767 (2008).
- [35] B. Sinha, Phys. Rep. **20**, 1 (1975).
B. Sinha and S. A. Moszkowski, Phys. Lett. B**81**, 289 (1979).
- [36] T. Furumoto, Y. Sakuragi, and Y. Yamamoto, Phys. Rev. C**82**, 044612 (2010).
- [37] K. Minomo, K. Ogata, M. Kohno, Y. R. Shimizu and M. Yahiro, J. Phys. G **37**, 085011 (2010) [arXiv:0911.1184 [nucl-th]].
- [38] R. Machleidt, K. Holinde K and Ch. Elster, Phys. Rep. **149**, 1(1987).
- [39] J. F. Berger, M. Girod and D. Gogny, Comput. Phys. Commun. **63**, 365 (1991).
- [40] W. Nazarewicz and A. Sobiczewski, Nucl. Phys. **A369**, 396 (1981).
- [41] T. Shoji and Y. R. Shimizu, Progr. Theor. Phys. **121**, 319 (2009).
- [42] S. Cwiok, J. Dudek, W. Nazarewicz, J. Skalski and T. Werner, Comp. Phys. Comm. **46**, 379 (1987).
- [43] M. Strutinsky, Nucl. Phys. **A122**, 1 (1968).
- [44] M. Brack, J. Damgård, A. S. Jensen, H. C. Pauli, V. M. Strutinsky, and C. Y. Wong, Rev. Mod. Phys. **44**, 320 (1972).
- [45] W. D. Myers and W. J. Swiatecki, Nucl. Phys. **81** 1 (1966); Ark. Phys. **36**, 343 (1967).
- [46] N. Tajima, Y. R. Shimizu, and S. Takahara, Phys. Rev. C **82** (2010), 034316.
- [47] P. Ring and P. Schuck, *The nuclear many-body problem*, Springer, New York (1980).
- [48] T. Ono, Y. R. Shimizu, N. Tajima and S. Takahara, Phys. Rev. C **82**, 034310 (2010).
- [49] S. Tagami and Y. R. Shimizu, to be published.
- [50] L.J. Tassie and F.C. Barker, Phys. Rev. **111**, 940(1958).
- [51] W. Horiuchi, Y. Suzuki, B. Abu-Ibrahim and A. Kohama, Phys. Rev. C **75**, 044607(2007).
- [52] M. Takechi, *et al.*, Phys. Rev. C **79**, 061601(R) (2009).
- [53] L. Chulkov *et al.*, Nucl. Phys. **A603** 219, (1996).
- [54] T. Suzuki *et al.*, Phys. Rev. Lett. **75**, 3241 (1995).
- [55] H. de Vries, C. W. de Jager, and C. de Vries, At. Data Nucl. Data Tables **36**, 495 (1987).
- [56] R. P. Singhal *et al.*, Nucl. Instr. and Meth. **148**, 113(1978).
- [57] W. G. Love and M. A. Franey, Phys. Rev. C**24**, 1073 (1981); M. A. Franey and W. G. Love, Phys. Rev. C**31**, 488 (1985).
- [58] M. Lacombe, *et al.*, Phys. Rev. C**21**, 861(1980).
- [59] <http://www.nnbc.bnl.gov/chart/>
- [60] B. Jurado, *et al.*, Phys. Lett. **B649**, 43 (2007).
- [61] G. Ausi, A. H. Wapstra, and C. Thibault, Nucl. Phys. A**729**, 337, (2003).
- [62] M. Kamimura, M. Yahiro, Y. Iseri, Y. Sakuragi, H. Kameyama, and M. Kawai, Prog. Theor. Phys. Suppl. **89**, 1 (1986).
- [63] N. Austern, Y. Iseri, M. Kamimura, M. Kawai, G. Rawitscher, and M. Yahiro, Phys. Rep. **154**, 125 (1987).
- [64] N. Austern, M. Yahiro, and M. Kawai, Phys. Rev. Lett. **63**, 2649 (1989).
- [65] N. Austern, M. Kawai, and M. Yahiro, Phys. Rev. C **53**, 314 (1996).
- [66] A. Deltuva, A.M. Moro, E. Cravo, F.M. Nunes, and A.C. Fonseca, Phys. Rev. C **76**, 064602 (2007).
- [67] K. Rusek and K.W. Kemper, Phys. Rev. C **61**, 034608 (2000).
- [68] J.A. Tostevin, F.M. Nunes, and I.J. Thompson, Phys. Rev. C **63**, 024617 (2001).
- [69] B. Davids, S.M. Austin, D. Bazin, H. Esbensen, B.M. Sherrill, I.J. Thompson, and J.A. Tostevin, Phys. Rev. C **63**, 065806 (2001).
- [70] J. Mortimer, I. J. Thompson, and J. A. Tostevin, Phys. Rev. C **65**, 064619 (2002).
- [71] K. Ogata, M. Yahiro, Y. Iseri, T. Matsumoto, and M. Kamimura, Phys. Rev. C **68**, 064609 (2003).
- [72] T. Matsumoto, E. Hiyama, K. Ogata, Y. Iseri, M. Kamimura, S. Chiba, and M. Yahiro, Phys. Rev. C **70**, 061601(R) (2004).
- [73] D.J. Howell, J.A. Tostevin, and J.S. Al-Khalili, J. Phys. G: Nucl. Part. Phys. **31**, S1881 (2005).
- [74] K. Rusek, I. Martel, J. Gómez-Camacho, A.M. Moro, and R. Raabe, Phys. Rev. C **72**, 037603 (2005).
- [75] T. Matsumoto, T. Egami, K. Ogata, Y. Iseri, M. Kamimura, and M. Yahiro, Phys. Rev. C **73**, 051602(R) (2006).
- [76] A.M. Moro, K. Rusek, J.M. Arias, J. Gómez-Camacho, and M. Rodríguez-Gallardo, Phys. Rev. C **75**, 064607 (2007).
- [77] M. Rodríguez-Gallardo, J. M. Arias, J. Gómez-Camacho, R. C. Johnson, A. M. Moro, I. J. Thompson, and J. A. Tostevin, Phys. Rev. C **77**, 064609 (2008).
- [78] M. Rodríguez-Gallardo, J. M. Arias, J. Gómez-Camacho, A. M. Moro, I. J. Thompson, and J. A. Tostevin, Phys. Rev. C **80**, 051601(R) (2009).
- [79] T. Matsumoto, K. Kato, and M. Yahiro, Phys. Rev. C **82**, 051602 (2010) [arXiv:1006.0668 [nucl-th]].
- [80] M. Avrigeanu and A.M. Moro, Phys. Rev. C **82**, 037601

- (2010).
- [81] W. Horiuchi, Y. Suzuki, P. Capel, and D. Baye, Phys. Rev. C **81**, 024606 (2010).
 - [82] W. Satula, J. Dobaczewski and W. Nazarewicz, Phys. Rev. Lett. **81**, 3599 (1998).
 - [83] T. Otsuka, T. Matsuo and D. Abe, Phys. Rev. Lett. **97**, 162501 (2006).
 - [84] S. Hilaire and M. Girod, Eur. Phys. J. A **33**, 237(2007).
 - [85] http://www-phynu.cea.fr/science_en_ligne/carte_potentiels_microscopiques/carte_potentiel_nucleaire_eng.htm
 - [86] K. Bennaceur, J. Dobaczewski, and M. Ploszajczak, Phys. Lett. **B496**, 154 (2000).
 - [87] K. Hagino and H. Sagawa, Phys. Rev. C **84**, 011303 (2011) [arXiv:1105.5469 [nucl-th]].